AD-A049 199 MARTIN MARIETTA LABS BALTIMORE MD F/G 20/4

BOUNDARY LAYER OVER SPINNING BLUNT-BODY OF REVOLUTION AT INCIDE--ETC(U)

1977 K C WANG F49620-76-C-0004

UNCLASSIFIED AFOSR-TR-77-1306 NL

1 OF 1

AD A049199

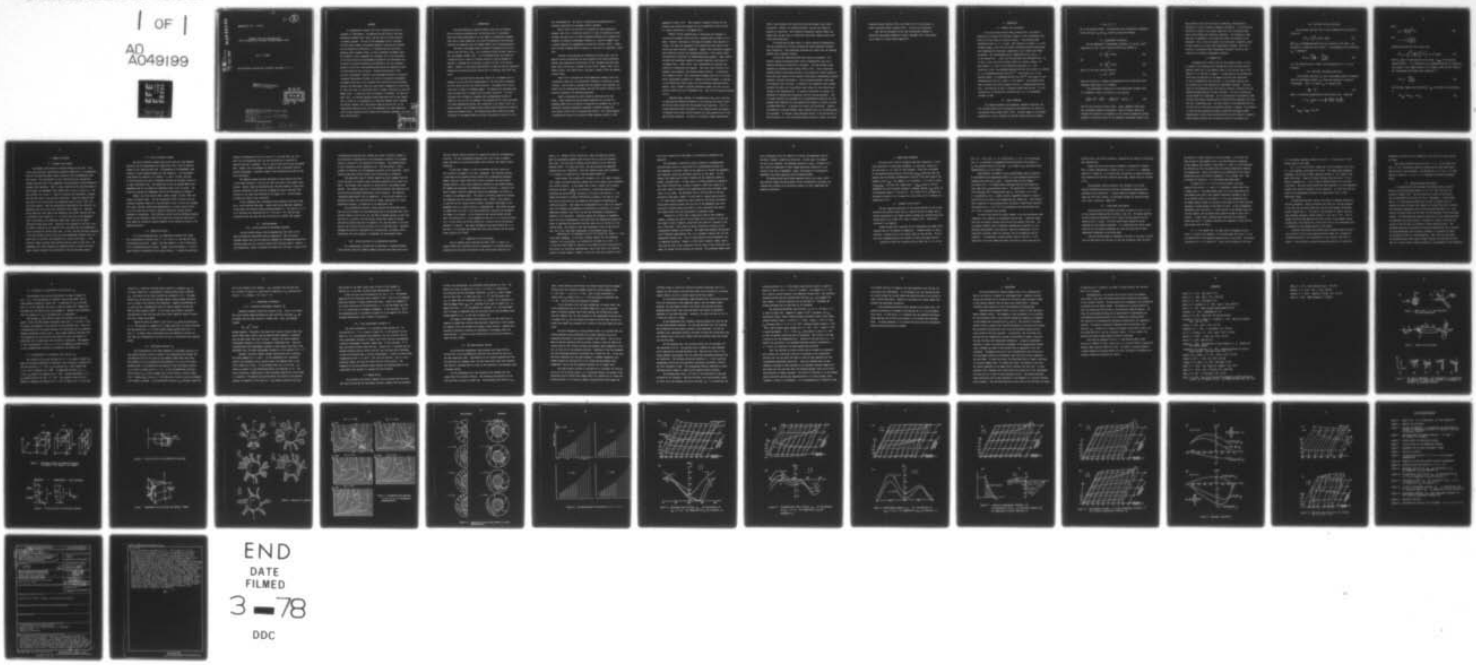

END

DATE FILMED

3-78

DDC

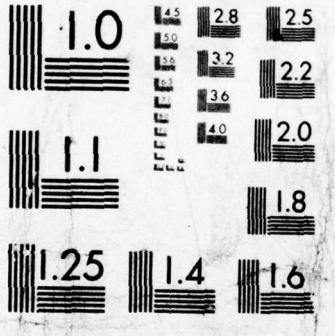

MICROCOPY RESOLUTION TEST CHART
NATIONAL BUREAU OF STANDARDS-1963-A

AD A049199

AD No.
DDC FILE COPY

(2)

AFOSR-TR- 77-1306

Boundary layer over spinning blunt-body of revolution at incidence including Magnus forces

By K. C. Wang

Martin Marietta Laboratories, Baltimore, Maryland, U. S. A.

Approved for public release;
distribution unlimited.

DDC
RECEIVED
JAN 31 1978
B

AIR FORCE OFFICE OF SCIENTIFIC RESEARCH (AFSC)
NOTICE OF TRANSMITTAL TO DDC
This technical report has been reviewed and is
approved for public release IAW AFR 190-12 (7b).
Distribution is unlimited.
A. D. BLOSE
Technical Information Officer

(See 1473)

ABSTRACT

An incompressible laminar flow over a spinning blunt-body at incidence is investigated. The approach follows strictly the three-dimensional boundary layer theory, and the lack of initial profiles is readily resolved. The rule of the dependence zone is satisfied with the Krause scheme, and complete numerical solutions are obtained for an ellipsoid of revolution at 6° incidence and two spin rates. Spinning causes asymmetry which, in turn, introduces the Magnus force. The asymmetry is most pronounced in crossflow, but is also noticeable in the skin friction and displacement thickness of the meridional flow. A variety of crossflow profiles are determined as are the streamline patterns in the cross- and meridional-plane which are especially useful in visualizing the flow structure. Detailed distribution of skin friction, displacement thickness, and centrifugal pressure are presented. A negative displacement thickness is found to be physically meaningful. The Magnus forces due to the crossflow skin friction and the centrifugal pressure are determined; these two forces partly compensate for each other. At lower spin rate, the frictional force is larger, resulting in a positive Magnus force. At high spin rate, the opposite is obtained. At high incidence (30°), the leeside separated region associated with an open separation is found not to be amenable to a classical boundary layer treatment. The present boundary layer calculations could be carried out, in the longitudinal direction, only up to the beginning of an open separation. Since an open separation moves forward with increasing incidence, the calculable area decreases.

Section ☑
ection ☐
☐

BY
DISTRIBUTION/AVAILABILITY CODES
Dist. AVAIL. and/or SPECIAL
A

1. INTRODUCTION

The three-dimensional laminar boundary layer over an inclined body of revolution spinning about its own major axis is considered. Aside from being interesting in its own right as a moving-wall boundary layer flow in three dimensions, this kind of problem has long attracted attention in connection with the "Magnus effect" for a flying projectile.

The idea of the Magnus effect is usually introduced in the literature as the lift force, $\rho\Gamma V_\infty$, on a rotating circular cylinder (figure 1a, see, for example, Prandtl 1952). It is presented within the context of a potential flow in terms of a uniform velocity V_∞ and an assumed circulation Γ, although the circulation is noted to be due to the viscous effect. However, it has always been difficult to make the precise connection between the circulation and the viscous flow (or boundary layer flow) very clear.

For an inclined finite long body (figure 1b), the Magnus force is defined to be the side force perpendicular to the lift plane (containing the lift vector and the free stream velocity). The moment due to such a side force is known as the Magnus moment. The Magnus force and moment may cause a flying object to depart from its preset trajectory. The cross-sectional view of figure 1b resembles the two-dimensional picture of figure 1a, but this way of looking at the problem does not really help much. In a three-dimensional problem, the circulation is not always a very convenient concept, and the Magnus forces could be better analyzed in terms of surface-distributed forces. The question about what surface force would contribute to the Magnus effects and their calculability turns out to be a

very challenging one. Our search to understand the mechanism and to determine quantitatively the Magnus effects continues.

Martin (1957), was the first to consider the three-dimensional boundary layer over a cylindrical portion of a body of revolution at small incidence and spin rate by a small perturbation method and to identify the asymmetry of boundary displacement thickness as a source of Magnus force. A similar approach was independently carried out by Kelley (1954). Sedney (1957) further extended Martin's analysis to the case of a supersonic, sharp cone.

Interest in this problem has resurfaced in recent years, and the method of small perturbations has been replaced by the finite-difference method, thus removing the restrictions of small incidence and small spin. Dwyer (1971) led the way, followed by Clark (1972), Vaughn & Reis (1973), Watkins (1973), Lin & Rubin (1974), and Dwyer & Sanders (1976) and Sanders & Dwyer (1976).

Dwyer (1971) calculated the three-dimensional boundary layer over a hypersonic sharp cone, but encountered difficulty in obtaining a unique solution. This led him to conclude that the boundary layer equations are invalid for the spinning-body problem, and that the lateral diffusion term should be retained in the governing equations.

Dwyer's contention was later shared by Clark and by Lin and Rubin. Clark adopted full Navier-Stokes equations for the case of a spinning sphere and an ellipsoid of revolution at incidence, but lack of sufficient resolution apparently presented a difficult problem and very sketchy results for the ellipsoid were givern. Lin & Rubin employed a parabolicized version of the Navier-Stokes equations similar to that

suggested by Dwyer (1971). They obtained a complete solution for the spinning cone problem and singled out the circumferential skin friction as a major contribution to the Magnus force.

Watkins (1973b) disputed Dwyer's conclusions and attempted to calculate the boundary layer flow over a spinning ogive-cylinder at incidence. Watkins' insistence on following the boundary layer approach is correct, but there are apparently other difficulties that make his work (which has scanty results) incomplete. Vaughn & Reis developed an approximate analytical solution for spinning projectiles. Their method should be particularly attractive for engineering design purposes. These authors included the centrifugal pressure as another important contribution to the Magnus force. Dwyer (1976), later reconsidered the spinning cone problem in collaboration with Sanders. This time, they returned to the boundary layer approach, and obtained unique solutions. In particular, they (Sanders & Dwyer 1976) calculated the Magnus force due to the asymmetric displacement thickness by a separate inviscid program, in contrast to the slender-body theory used by all the previously mentioned authors. However, Dwyer & Sanders' modified difference scheme still does not completely satisfy the rule of dependence zone. This will be discussed further in §3.5.

Spinning causes reversal of circumferential flow, and it has been an open question whether calculation of such reversed flow would violate the initial-value concept for the boundary layer equations. Lack of a strong theoretical basis contributes to the confusion about the adequacy of boundary layer theory and the necessity of using parabolicized or full Navier-Stokes equations. Of course, in principle, higher approximation

offers a more complete flow description than the boundary layer theory can provide. However, for specific purposes, this may not always be necessary or desirable. More elaborate formulation requires longer computing time, and may lead to insufficient resolution, making results unreliable and inconclusive.

In related work by Wang (1975), a similar reversed circumferential flow was calculated by strictly following the three-dimensional boundary layer formulation. This experience convinced this author that the spinning problem can be similarly treated.

In this work, detailed methods and results are presented. The specific problem investigated deals with an incompressible flow over a spinning ellipsoid of revolution at incidence. The same problem without spinning was considered ealier (Wang 1974a,b; 1975). Such a blunt-body problem provides interesting contrasts to the previously studied supersonic sharp cone case because of the presence of meridional (longitudinal) pressure gradients, favorable and adverse. Lack of pressure gradients would mean less boundary layer variation. §2 describes the formulation which remains basically the same as in the previous work, except for those features pertaining to the spinning motion. §3 explains the method of solution, the rationale of reversed-flow calculation, and the starting procedure. Lack of initial profiles was considered as an insurmountable difficulty for the boundary layer approach, but this question can actually be readily resolved as demonstrated here. §4 presents the results and discussions. Complete distributions of various boundary layer characteristics on the spinning-body are presented. In contrast, other published results of the distribution of skin frictions, e.g., for the pointed bodies previously studied, are either

completely absent (Watkins 1973b, Lin & Rubin 1974) or only given at a single crossplane (Dwyer & Sanders 1976). §5 gives the conclusions.

This work was presented at the 14th International Congress of Theoretical and Applied Mechanics at Delft, September 1976. More details can be found in a recent report (Wang 1977).

2. FORMULATION

2.1 Geometry and coordinates

As in the previous study by Wang (1974a,b;1975), the specific example of an ellipsoid of revolution (figure 2) with a minor/major axes ratio of 1/4 was chosen for concrete results. A non-rotating body-coordinate system, μ, θ, z is used. With reference to figure 2, α is the incidence angle, μ and θ are two surface coordinates along the meridional and circumferential directions, respectively, and z denotes the normal coordinate. The corresponding metric coefficients are h_μ and h_θ. e is the eccentricity. a and b are the semi-major and semi-minor axes. h_θ, in fact, is just the cross-sectional radius at a fixed μ-station. We shall denote u, v, and w as the velocities along the μ, θ, and z directions; u and v are nondimensionalized with the flow velocity at infinity V_∞; w is nondimensionalized with $V_\infty/R^{1/2}$, where $R(=V_\infty a/\nu)$, is the Reynolds number; z is nondimensionalized with $a/R^{1/2}$; the pressure is non-dimensionalized with ρV_∞^2, where ρ is the density. The ellipsoid spins about its major axis with an angular velocity ω nondimensionalized with V_∞/a. The direction of spin is clockwise viewed from the rear. All the variables are in the physical, primitive form; i.e., no transformed variable is used.

2.2. Basic equations

The complete boundary layer equations, boundary conditions, and the inviscid solution for an ellipsoid of revolution are the same as in the previous work by Wang (1974a, 1975). The only change in the boundary conditions is in the v-velocity at the body surface which now becomes:

$$v = \omega h_\theta \quad \text{at } z = 0$$

due to the spinning motion. The meridional and circumferential components of skin friction, $c_{f\mu}$ and $c_{f\theta}$, remain as previously defined.

2.3. Displacement thicknesses

The two components of displacement thickness, Δ_μ^* and Δ_θ^*, based respectively on the u- and v-velocity profiles are defined by

$$\Delta_\mu^* = \frac{1}{q}\int_0^\infty (U-u)dz, \tag{1a}$$

and

$$\Delta_\theta^* = \frac{1}{q}\int_0^\infty (V-v)dz, \tag{1b}$$

where q is the total inviscid velocity,

$$q = (U^2 + V^2)^{1/2}. \tag{1c}$$

These are written in a slightly unconventional form to facilitate their evaluation when either U or V vanishes.

The displacement thickness of a three-dimensional boundary layer Δ^* is defined in terms of Δ_μ^* and Δ_θ^* by the equation:

$$\frac{\partial}{\partial\mu}\left[h_\theta\,(U\Delta^* - q\Delta_\mu^*)\right] + \frac{\partial}{\partial\theta}\left[h_\mu(V\Delta^* - q\Delta_\theta^*)\right] = 0. \tag{1d}$$

This was first derived by Moore (1953). Later, Lighthill (1958) gave four alternative methods of derivation. Moore's original method was included and referred to by Lighthill as the "velocity comparison" method. Lighthill's derivation relies on the streamline coordinates formed by the

equi-potential lines and the inviscid streamlines, whereas Moore's derivation is valid in general orthogonal coordinates. A new alternative derivation is given by this author (Wang 1977) and is patterned after that of the ordinary mass continuity equations. The reasoning is somewhat akin to Lighthill's "flow reduction" method, but differs in the formalism. Also, it does not depend on the particular coordinate system. We shall refer to Δ^* as the total displacement thickness, Δ_μ^* as the u-velocity (or meridional flow) displacement thickness, and Δ_θ^* as the v-velocity (or crossflow) displacement thickness.

2.4 Magnus Force

The Magnus force results from the flow asymmetry which, in turn, is caused by the spinning motion through the action of fluid viscosity. Symmetry refers here to the symmetry plane of the inviscid flow or the plane of $\theta = 0°$ and $180°$ in figure 2. As mentioned in the Introduction, three major contributions to the Magnus force have been identified: (1) the circumferential skin friction, (2) centrifugal pressure, and (3) pressure due to the asymmetrical displacement thickness. Only the first two are determined here; the third one requires a separate inviscid computing program and has not been calculated. Two other contributions are also known to be important: one is concerned with the asymmetric wake vortices shed from an inclined body of revolution which generate side-force even for a nonspinning case. The other relates to the separated flow over the aft-body for which even a qualitative picture is lacking. The asymmetry of such aft-body separated flow affects especially the Magnus moment. Determination of those wake vortices and the tail flow requires a complete Navier-Stokes solution, and is beyond the scope of the present work.

2.4a. Sectional friction side-force

The sectional side-force due to the circumferential skin friction is given by

$$\sqrt{R}\, F_{sf} = -\int_0^{\infty} \sqrt{R}\, c_{f\theta} \cos\theta \; h_\theta d\theta), \tag{2a}$$

where F_{sf} is nondimensionalized with ρV_∞^2, positive to the right. The subscript, sf, stands for skin friction. A corresponding force coefficient, c_{sf}, is defined by

$$\sqrt{R}\, c_{sf} = \frac{\sqrt{R}\, F_{sf}}{\text{area}} = \frac{\sqrt{R}\, F_{sf}}{\pi (b/a)^2}, \tag{2b}$$

i.e., the reference area is taken to be the midsection ($\mu = 0$) of the ellipsoid.

2.4b. Sectional centrifugal side-force

The sectional side-force F_{ct} due to centrifugal effects is obtained from the centrifugal pressure, p_{ct}, where the subscript ct stands for "centrifugal". After v is known, p_{ct} is evaluated from

$$\frac{\partial p}{\partial y} = \frac{v^2}{y}, \tag{3a}$$

where y is measured perpendicularly from the major axis. Replacing

$$y = h_\theta + \frac{z}{\sqrt{R}} \operatorname{Cos} \phi \simeq h_\theta, \quad \frac{\partial p}{\partial y} = \frac{\partial p}{\partial z}\frac{\partial z}{\partial y} = \frac{\partial p}{\partial z}\frac{\sqrt{R}}{\cos \phi}$$

then

$$p_{body} = p_{edge} + p_{ct}/\sqrt{R},$$

where

$$p_{ct} = -\frac{\cos\phi}{h_\theta}\int_0^\infty v^2\, dz, \tag{3b}$$

with

$$\phi = \sin^{-1}\left(\frac{\partial h_\theta}{h_\mu \partial\mu}\right) .$$

Integrating around the cross section gives

$$\sqrt{R}\, F_{ct} = -\int_0^{2\pi}\left[-\frac{\cos\phi}{h_\theta}\int_0^\infty v^2 dz\right] (\sin\theta)\ (h_\theta d\theta) , \tag{3c}$$

where F_{ct} again is taken positive to the right. P_{edge} is the inviscid surface pressure. It is unaffected by the spinning motion and is symmetrical with respect to the symmetry-plane so its integral around the body vanishes. The corresponding centrifugal force coefficient is

$$\sqrt{R}\, c_{ct} = \frac{\sqrt{R}\, F_{ct}}{\pi(b/a)^2} . \tag{3d}$$

The sectional, Magnus force coefficient, c_{Mg}, from these two contributions is

$$\sqrt{R}\, c_{Mg} = \sqrt{R}\, c_{sf} + \sqrt{R}\, c_{ct}. \tag{3e}$$

3. METHOD OF SOLUTION

3.1. Boundary layer method

The boundary layer method is followed through in this work. This choice comes naturally from previous experience (Wang 1975) in a nonspinning case for the same body where similar reversal of the circumferential flow also occurs. The calculability of such reversed flow was rationalized, thereby using the rule of the dependence zone pertaining to three-dimensional boundary layer equations. What is really involved can be seen from figure 3, which depicts the dependence zone (shaded area) in the μ-θ plane (i.e., the body surface) for a point P. Figure 3a indicates the coordinates, assuming that the body spins in the positive θ-direction. Figure 3b indicates that when there is no flow reversal, the dependence zone of point P falls into the third quadrant. When the nonspinning circumferential flow reverses, the dependence zone lies across the μ-coordinate line (figure 3c). Spinning merely makes the lower edge of the dependence zone almost coincide with the θ-coordinate lines (figure 3d, e). As long as the rule of the dependence zone is satisfied by the difference scheme used, there are no logical differences among these cases. Reversal of one component of the flow is not the same as reversal of the resultant flow, and hence does not automatically lead to violation of initial-value idea. In fact, the flow direction (parallel to the body surface) varies across the three-dimensional boundary layer at a given point on the body, thus sweeping out a certain solid angle. A distinctive, single resultant flow direction does not exist in this case. The dependence rule, which requires the computation mesh to enclose the solid angle, ensures precisely the satisfaction of the initial-value concept.

3.2. Finite difference schemes

The finite difference schemes used in this work are those employed previously for the nonspinning case (Wang 1974a, 1975); they are implicit schemes of the Crank-Nicolson type. Corresponding to the dependence zones of figure 3, three different meshes are used (figure 4). For convenience, these meshes are referred to as schemes 1, 2, and 3. In each, the data at the solid points are used to determine solutions at the empty circles in a single calculation step. The shaded area on the top surface denotes the dependence area of the respective computation mesh in the μ-θ plane. The latter must enclose the dependence area of the flow depicted in figure 3.

Scheme 1 was first used by Dwyer (1968); scheme 2 by Hall (1967) and scheme 3 by Krause (1969). For the calculation of the w-velocity from the continuity equation (Wang 1975), the derivative, $\partial w/\partial z$, at first was averaged over corner stations (rather than approximated at a single central station as in this work) and was found to exhibit fluctuation, causing eventual breakdown of calculation. Such difficulty results from the difference approximation for the continuity equation and hence falls beyond the prediction of usual numerical instability analysis applied to the linearized version of the momentum equations.

3.3 Computation details

As in the nonspinning cases, our computation proceeds first along the circumferential direction from $\theta = 0$ to π and to 2π, and then aft along the meridional direction. Scheme 1 was used between $\theta = 0$ and π where there is no circumferential-flow reversal. Scheme 3 was used between $\theta = \pi$ and 2π where reversed circumferential flow always prevails. It should be noted that

reversed circumferential flow also occurs at θ less than 180° (say 120° ∿ 180°) for the nonspinning case, but such reversed flow is annulled by opposite flow due to spinning. This is true at least for the case calculated here. Scheme 1 has the advantage of simplicity and is available from our previous development. Otherwise, scheme 3 can alternatively be used for the whole calculation.

The computer program has been developed to allow various step sizes in the normal direction z, but only two sizes were used in the present calculations. Smaller steps were maintained near the body surface to ensure more accurate evaluation of skin friction, although the results show that skin friction is not really much affected by the change of Δz. On the average, 50 steps were taken in the z-direction.

To save computing time, experiments using different step sizes along the μ- and θ-direction were made. Larger steps can be employed, depending on how severe the relevant adverse pressure gradient is. The case of $\omega = 1.0$ at 6° incidence was calculated with $\Delta\mu = 0.05$ and $\theta = 10°$, and the whole calculation took less than one hour of CPU time on a UNIVAC 1108 computer.

3.4. Starting methods

3.4a. Initial profiles for meridional marching

Initial profiles along a fixed crossplane near the vertex of the body are needed for meridional march of computation. Near the vertex, spinning effects have not yet materially changed the corresponding nonspinning profiles except for the v-velocity profile near the body surface. Based on this observation, initial u-profiles were taken to be the same as those of the

corresponding nonspinning case, whereas the initial v-profiles (figure 5) were obtained by superposition of the nonspinning v-profiles on an assumed profile to account for the spinning of the boundary. The assumed profile in this calculation was an exponential one. With the initial u- and v-profiles so obtained, the corresponding w-profiles can be calculated. Calculations using these initial profiles were started with no difficulty.

This experience tends to further support the usual argument that the initial profiles for boundary layer calculation generally do not have to be exact. The boundary layer problem is a mixed initial- and boundary-value problem. The boundary-value part of the problem provides some capability for self-correcting reasonably-approximated initial profiles. The adjective "reasonably-approximated" must be emphasized. If the initial profiles are arbitrarily picked, the calculation may be doomed, particularly for three-dimensional problems, in comparison to two-dimensional ones.

In the pointed-body problem, initial profiles for meridional march near the tip are taken to be the nonspinning ones on the grounds that, since the body radius is zero at the tip, the body's spinning velocity is also zero. The fact is, of course, that the initial station must always be located some finite distance away from the geometric tip, and the radius is not only nonzero, but also may even be not small, as in a blunt-body case. Therefore, although this method is reasonable for a pointed body, our method, with a modification for pure spinning, is preferable for more general bodies.

3.4b. Initial profiles for circumferential marching

For a nonspinning, inclined body of revolution, a separate boundary layer solution along the windward symmetry plane has often been used to pro-

vide the required initial profiles for computation along the circumferential direction. For the corresponding spinning case, lack of such a symmetry plane, and hence its associated boundary layer solution, has caused a major difficulty.

In this work, scheme 2 is used to determine the first station at $\theta=0°$ (station 4 in figure 6) of a new crossplane. The resulting solution is then used as the required initial profile for circumferential marching. Scheme 2 does not require known data on the μ-constant line which passes through station 4, and is hence especially suitable for the present purpose. The shaded area represents the dependence zone of station 4. Obviously, the mesh of scheme 2 does not completely enclose the dependence zone unless $\Delta\mu$ is taken to be extremely small. The latter is certainly impractical because the computing time will become exceedingly long. However, since scheme 2 is used only at this single initial station, incomplete fulfillment of the dependence rule at a single station is inconsequential. Some effort was made to remedy this, but later it was found unnecessary, and hence was abandoned. The remedy is as follows: As the calculation was carried around the body once, the solution for $\theta = 0$ was compared to that for $\theta = 2\pi$, and the solution of $\theta = 2\pi$ was used as an initial profile for a second round of calculations between $\theta = 0$ and 60°. Only small differences were found between the $\theta = 0$ and the $\theta = 2\pi$ solutions and between the first round solution and the second round solution for $0° < \theta \leq 60°$.

3.5. Comparison with other methods

Lack of symmetry-plane solutions led Dwyer (1971) to resort to a "guess" method with iteration, which was considered to be semisatisfactory, excepting only that some oscillations in the results were found near the

plane $\theta = 0$. Watkins (1973a) carried out a small perturbation solution about the nonspinning symmetry-plane solution that is valid for moderate spin rates. This was used to develop initial profiles in his later work (Watkins 1973b). For large spin rates, the same solution was suggested, coupled with cyclic iterations. Since only sketchy results were presented, it is difficult to judge how this starting method worked out.

Other authors (Lin & Rubin 1974, Kitchens et al. 1975, Dwyer & Sanders 1976) sought to develop difference schemes that do not require such circumferential initial profiles. In the scheme used by Dwyer & Sanders the crossflow derivative operator ($v \frac{\partial}{h_\theta \partial\theta}$ in our notation) is always kept positive by evaluating the derivative $\frac{\partial}{\partial\theta}$ according to the sign of the velocity v. Such change from forward to backward differencing according to the sign of v has been used in inviscid flow, and indeed has the property of modelling the convection properly. What should be distinguished here is that in an inviscid flow, the influence and depnedence are determined by convection; in a three-dimensional boundary layer flow, the same are determined by diffusion in addition to the convection. Diffusion spreads the influence or dependence across the layer instantaneously, and hence blurs the demarcation between the layers of opposing flow-direction from what would occur on the basis of convection along. The outcome is that this technique is valid in the inviscid case, but is not valid when transplanted to the boundary layer case.

Schematically, the dependence zone for the station AA_2 (figure 7) is the whole wedge $AA_2BB_2DD_2$. In the Dwyer & Sanders scheme, only two subwedges, $AA_1BB_1CC_1$ and $A_1A_2C_1C_2D_1D_2$, are accounted for (Kitchens et al 1975). It is true that their scheme is implicit in the normal direction along which all grid points are calculated simultaneously; and in this sense, the diffusive nature is loosely modeled. However, it does not seem that an implicit calcu-

lation would supplant the requirement of satisfying the dependence rule completely.

The advantage of requiring no initial values for circumferential-direction march would be a great asset for a spinning-body problem, but such advantage is seriously offset by the inability to satisfy the dependence rule completely unless the meridional step size is very small. In this respect, the scheme used by Dwyer & Sanders has the identical problem as scheme 2 discussed above. In both cases, no initial profiles are needed in the lateral direction and, as shown in figure 6, there will always be an area which cannot be covered by the computation mesh unless extremely small steps, $\Delta\mu$, are taken. The difference lies in the fact that in the case presented in this paper, scheme 2 is only used at a single point-station at $\theta = 0°$, while Dywer & Sanders use their scheme for the entire calculation. These authors mention further that the rule of the dependence zone could be grossly violated without much effect on their calculation and results. This author doubts that this prescription is generally valid.

Kitchens et al.(1975) made a comparative study of four different schemes, including the earlier version (Wang 1974a) of scheme 2 (§3.4b) and the scheme of Dwyer & Sanders; calculations were made for a parabolic flow over a flat plate. Their study was mainly motivated by interest in the spinning-body boundary layer problem. The scheme they proposed incorporated Lax's difference approximation (see, e.g., Richtmyer & Morton 1967) for one-dimensional unsteady flow. This is a good feature, and the dependence rule is completely satisfied. However, as with Dwyer & Sanders' scheme, theirs also uses one step in the μ-direction, and two steps in the θ-direction, and, again, no lateral initial-profiles are required. The preceding comment about

such an advantage versus the inability to satisfy the dependence zone for the Dwyer & Sanders' scheme also holds here. In both cases, the penalty one has to pay outweighs the advantage received in return. Kitchens et al. also stress the importance of their scheme being more insensitive to violations of the zone of dependence. Again, the necessity of violating the dependence rule arises precisely from the adopted scheme.

The parabolicized Navier-Stokes approach used by Lin & Rubin (1974) also does not require initial profiles in the circumferential direction; but treating the crossflow in an elliptical fashion is a more complicated and expensive alternative.

4. RESULTS AND DISCUSSION

Two cases with 6° and 30° incidence have been calculated to illustrate solutions at low and high incidences. In each case, results for two spin rates (ω = 0.5 and 1.0) were obtained. These rates correspond to the maximum spinning velocity of the body $(v_B)_{max}$ being less than and greater than the maximum circumferential velocity at the outer edge of the boundary layer, V_{max}. For example, at 6° incidence, ω = 0.5 and 1.0 gives $(v_B)_{max}/V_{max}$ = 0.64 and 1.28, respectively. $(v_B)_{max}$ occurs at the mid-body where the cross-sectional diameter is maximum; whereas, V_{max} occurs in the meridional planes θ = 90° and 270°. The results for 6° incidence are presented in detail in §4.1 through §4.8; the results of 30° incidence are summarized in §4.9.

4.1. Boundary layer profiles

The most important quantities in the present problem are the circumferential-flow profiles which take on a greater variety of shapes than is usually encountered in any single problem including the spinning sharp cone studied before (Lin & Rubin 1974, Dwyer & Sanders 1976). Figures 8a-e illustrate a few examples.

Figure 8a gives the v-profiles for the nonspinning case (Wang 1975), included here for the purpose of comparison. A symmetry plane is clearly indicated. Reversed flow on the leeside occurs on the aft-body. The profiles are nondimensionalized with respect to local outer-edge velocity.

Figures 8b-d show the v-profiles with the spin rate ω = 0.5 on the

fore- (μ = -0.80), mid- (μ = 0), and aft-body (μ = 0.5). For the spinning case, it is convenient to nondimensionalize the profiles with respect to v_B, the spinning velocity of the body. v_B is equal to ωh_θ, and hence varies longitudinally as h_θ for a fixed ω.

Qualitatively, the source of these profile shapes can be visualized by superimposing the nonspinning profile on a pure spinning profile and by comparing the velocities v_B and V. Consider figure 8d, for example -- the profile for θ = 20° monotonically decreases from the body toward the outer edge with v_B being greater than V. The profile for θ = 90° monotonically increases with V being greater than v_B. The profile of θ = 140° is non-monotonic, but is always positive, apparently because a strong reversed flow occurs there in the nonspinning case (figure 8a). Such reversed flow is opposite to the spinning motion, and hence is effectively cancelled. The profiles for θ = 220°, 270° are non-monotonic and reversed while that of θ = 340° is monotonic and reversed.

In view of the variety of profile shapes, we use the descriptive words "monotonic" and "reversed" to distinguish various cases. "Reversed" means here that the profile contains both positive and negative velocities. One can readily identify cases of different combinations of monotonic or non-monotonic and reversed or non-reversed. Some are non-monotonic, but not necessarily reversed; others are reversed, but can be monotonic and non-monotonic. A non-monotonic reversed profile (such as that for θ = 220°, figure 8d) is not very common and occurs only where a strong reversed flow

already exists, even without spinning. Spinning has the effect of reinforcing such reversed flow.

Higher spin rates exert greater influence in shaping the v-profile. This is clearly demonstrated in figure 8e for $\omega = 1.0$ at $\mu = 0$. Comparing figure 8e to figure 8c, it is evident that all profiles in figure 8e monotonically decrease from the body toward the outer edge, whether they are reversed or not.

The meridional velocity profiles, the u-profiles, do not show features differing particularly from the corresponding nonspinning ones, and hence are not shown here. A certain degree of asymmetry between the right and left sides, however, is noticeable through the coupling between the u- and v- velocities (Wang 1977).

4.2. Cross-plane flow pattern

The cross-plane flow patterns are shown in figures 9a-e for $\omega = 1.0$ at five stations extending from the front to the rear. The arrows indicate the flow direction determined by $\tan^{-1}(h_\theta w/v)$ and the patterns are presented in the θ, z plane. The solid curves drawn through the arrows represent the cross-plane streamlines. It is understood that these streamlines are not the actual streamlines, but only the projection of three-dimensional streamlines on the cross-plane.

The most obvious effect of spinning is that due to viscosity, the flow near the body spins with the body, so that the streamlines (near the body)

are parallel or nearly parallel to the body surface. In contrast, the outer portion of the boundary layer is not much affected by spinning, so that symmetry with respect to the planes $\theta = 0$ and π is still preserved. The structure of the cross-plane flow can be better analyzed by studying the singularities. These are located at the intersection of the curves, along which one of the velocity components, v or w, becomes zero. They are denoted in figures 9a - e by the dotted and broken lines.

In Figure 9a for $\mu = -0.90$ (on the fore-body), the intersection of the curves, $v = 0$ and $w = 0$, determines a nodal point N and a saddle point S. The nodal pattern near N is in the outer portion of the boundary layer and is only slightly affected by spinning so that N is not located exactly on the plane $\theta = \pi$ as in the nonspinning case. The saddle pattern around S is located in the middle of the fluid flow and represents a unique feature of the effect of spin. In the corresponding nonspinning case, the curve $v = 0$ would consist of the symmetry plane and the body surface, and the saddle point would be located at their intersection. In other words, spinning motion makes the flow asymmetric, shifts the curve $v = 0$ upwards, and moves the singularity S away from the body surface into the fluid.

At $\mu = -0.60$ (figure 9b), the nodal point N disappears and the curve $w = 0$ splits into branches. On the other hand, the curve $v = 0$ and the saddle point S are displaced upward and also to the right. Such trends continue up to $\mu = 0.2$ (figure 9c). Here, the two branches of the curve

$w = 0$ are further separated, whereas the curve $v = 0$ and the point S shift farther upward to the right.

At $\mu = 0.4$ in the aft-body (figure 9d), the two branches of the curve $w = 0$ join together at the upper left corner. The saddle point disappears altogether, and the flow becomes completely outward ($w > 0$), except at the upper left corner. Figure 9e further indicates that the curve $w = 0$ completely disappears at $\mu = 0.50$ so that an outflow prevails over the entire cross-plane. Such pure outflow would have been impossible in a two-dimensional cylinder flow from the viewpoint of mass continuity. It could occur here because of the accompanying meridional (or longitudinal) flow, a three-dimensional effect.

At downstream aft-body stations, the effect of spinning becomes more and more pronounced. Among the features that show this, the most apparent is the fact that the layer which spins with the body becomes increasingly thicker (figures 9d, e). The layer of such parallel (or nearly parallel) flow increases especially rapidly between $\theta = 180°$ and $\theta = 270°$. This is because the flows from opposite directions collide in that angular region. In particular, the reversed flow, which occurs even in the nonspinning case, is reinforced by the spinning motion in that region.

The above cross-plane flow patterns may be redrawn around the body's cross sections to give a more physical picture (figure 10), although the streamline patterns in this presentation is less accurate than those in figure 9. The previously calculated nonspinning patterns are included for

comparison, and since they are symmetrical, only half their cross sections are shown.

The results presented thus far are for $\omega = 1.0$. For the lower spin rate ($\omega = 0.5$), the general trends are similar and the layer which spins with the body is less noticeable. The pattern for $\omega = 1.0$ at $\mu = 0.2$ looks similar to that for $\omega = 0.5$ at $\mu = 0.4$, implying a lag from the spinning effect.

4.3. Meridional-plane flow pattern

In conjunction with the preceding cross-plane patterns, the flow patterns in fixed meridional planes ($\theta = 0°$, $90°$, $180°$, and $270°$) are plotted in figures 11a-d. The flow direction is given by $\tan^{-1}(h_\mu w/u)$ and is represented by the arrows in the μ,z coordinates. A curve, along which $w = 0$, could have been added (but was not) in figures 11a-d to separate the area of inflow (with respect to the body) from that of outflow. The calculated longitudinal flow is always pointed downstream (i.e., $u>0$). From the fore-body toward the aft-body, the flow generally turns increasingly outward. The meridional-plane patterns shown here are less complicated than the preceding cross-plane patterns. Decrease of ω tends to alleviate the outflow in the aft-body; but otherwise, similar patterns prevail. The meridional-plane and cross-plane flow patterns together help one to visualize the three-dimensional flow structure, although it is difficult to depict the streamline patterns in three-dimensions. When both the cross-plane and meridional-plane flows become strongly outward, the resultant flow also must be a strong outflow, leading inevitably to the beginning of flow separation.

4.4. Meridional (or longitudinal) skin friction, $c_{f\mu}$

The meridional skin friction distribution is shown in figure 12a for $\omega = 0.5$. This distribution is symmetric over the fore-body, but becomes gradually asymmetric farther aft. A comparison for $c_{f\mu}$ at the mid-body ($\mu = 0$) for different spin rates is shown in figure 12b. Higher spin rate makes the distribution even more asymmetric. However, the contribution from the asymmetry of $c_{f\mu}$ to the Magnus force is negligible.

The minimum $c_{f\mu}$ curve shown in figure 12a indicates that this component of skin friction becomes vanishingly small near $\mu = 0.55$ and $\theta = 310°$. This marks the beginning of the reversal of the meridional flow. Since the circumferential flow is already reversed, the calculation must be terminated whenever meridional reversal starts. Other common symptoms associated with flow separation were also noted at the juncture so that the reversal of meridional flow is taken here to be the onset of separation. What happens is that starting from $\theta = 310°$ at $\mu = 0.55$, the separation spreads quickly in the circumferential direction as indicated by the broken line.

4.5 Circumferential (or crossflow) skin friction, $c_{f\theta}$

The variation of $c_{f\theta}$ over the body for $\omega = 0.5$ is shown in figure 13a, which can be better understood by referring to the v-profiles in figures 8b-d. Over the fore-body ($\mu = -0.90$), $c_{f\theta}$ is positive for $\theta < 180°$ (except near $\theta = 0°$); but is negative for $\theta > 180°$. At downstream stations (e.g., $\mu = -0.60$), $c_{f\theta}$ begins to be negative for $\theta < 180°$. Farther downstream ($\mu > 0$), $c_{f\theta}$ becomes positive for $180° < \theta < 360°$. This change of sign can be explained by comparing the profiles for $\theta = 210°$ in figures 8c,d. In one case

(figure 8c), a monotonic reversed profile results in a negative $c_{f\theta}$; in the other (figure 8d), a non-monotonic reversed profile gives a positive $c_{f\theta}$. The reason for the latter profile was discussed in §4.1. The large positive $c_{f\theta}$ in the area just discussed implies strong reversed crossflows and is related to the eventual flow separation. Complete distributions of $c_{f\mu}$ and $c_{f\theta}$ over a spinning-body (such as those in figures 12a and 13a) have not been available before. For the sharp cone problem, calculated distributions of skin frictions have been either completely absent or given only for a single cross-plane.

Figure 13b shows the effect of spin rate on $c_{f\theta}$ along the midsection, $\mu = 0$. The increase of asymmetry due to higher spin rate is clearly indicated. The distribution for $\omega = 0.5$ falls roughly midway between those for $\omega = 0$ and 1.0. An almost linear relationship like this apparently reflects the fact that the circumferential flow near the body is controlled by the spinning motion.

4.6. Centrifugal pressure, p_{ct}

The circumferential flow always generates a centrifugal pressure, but this induced pressure causes no concern in the nonspinning case because the contributions from the two sides of the symmetry plane cancel each other. The asymmetry of the circumferential-flow profiles (§4.1) due to the body's spinning leads to an asymmetrical distribution of the centrifugal pressure, p_{ct} as shown in figure 14a for $\omega = 0.5$. In the circumferential direction, the variation of p_{ct} follows roughly that of the inviscid v-velocity (Wang 1975). Maximum $|p_{ct}|$ occurs at $\theta = 90°$ where the v-velocity across the boundary layer reaches a maximum. In the meridional direction, p_{ct} increases toward the

rear as the boundary layer thickens. $|p_{ct}|$ increases with the spin rate as is evident in figure 14b, which shows a comparison of p_{ct} along the mid-section, $\mu = 0$, between $\omega = 0.5$ and $\omega = 1.0$.

4.7. Displacement thicknesses

4.7a. v-Velocity displacement thickness, Δ_θ^*

Spinning introduces certain new features in Δ_θ^*. First, it is noted that Δ_θ^* can become negative because the flow velocity on the body, v_B, can be greater than the outer velocity V (figure 15b). Thus, the defining integral

$$V\Delta_\theta^* = \int_0^\infty (V-v)dz$$

becomes negative. Physically, this means that viscosity causes a mass flow excess rather than a defect, and the effective body boundary is displaced into the body rather than into the fluid. However, the idea of negative displacement thickness is only of conceptual significance here. Since the circumferential-flow displacement thickness is much smaller than that of the meridional flow, the total displacement thickness is still positive for $\alpha = 6°$.

Secondly, the above integral becomes indeterminate when V vanishes. The latter happens at $\theta = 0$ and π. In the nonspinning case, vanishing V leads to the vanishing of the v-profile across the boundary layer, so Δ_θ^* can be simply set to zero. In the spinning case, this is not true. q is chosen to replace V as the normalizing factor (see equations 1a, b). The latter introduces a complication in that Δ_θ^* becomes negative for $\pi<\theta<2\pi$ where V is negative. The negative Δ_θ^* discussed above for positive V has physical meaning; the negative Δ^* here does not. This awkward situation could have

been avoided if one added a minus sign in front of the integral in equation 1a, b; but then, Δ_θ^* would become discontinuous at $\theta = 180°$.

Figure 15a gives the distribution of Δ_θ^* for $\omega = 0.5$. The maximum magnitude in the θ-direction occurs around $\theta = 270°$. This is to be expected physically because of strong reversed flow there. Figure 15c compares Δ_θ^* for various spin rates at the mid-section, $\mu = 0$, with the higher spin rate ($\omega = 1.0$) causing Δ_θ^* to be negative throughout. To be consistent, Δ_θ^* for the nonspinning case is considered in figure 15c to be negative for $\pi \leq \theta \leq 2\pi$, although conventionally this is taken to be positive.

4.7b. Total displacement thickness, Δ^*

The total displacement Δ^* is calculated using equation 1d. Its distribution for $\omega = 0.5$ is shown in figure 16a. At the present low incidence ($\alpha = 6°$), the meridional flow dominates over the crossflow, and the total displacement thickness Δ^* differs very little from the corresponding u-velocity displacement thickness (figure 16b). On the fore-body, Δ^* is small and nearly uniform around the body. Farther aft, Δ^* increases and the maximum thickness position shifts from 180° into the direction of spinning, so that the displaced body is twisted longitudinally. Figure 16a shows slight irregularities near $\theta = 0°$ and $\theta = 180°$ over the aft-body. This is a computational effect, but does not affect the rest of the results. The asymmetry of the Δ_μ^* distribution again reflects the spinning effect on the longitudinal flow through its coupling with the crossflow.

4.8 Magnus forces

The sectional side-forces or Magnus forces resulting from the crossflow skin friction and the centrifugal pressure, together with the resultant

of these two contributions, are calculated using equations 2b, 3d-e. The results are shown in figures 17a, b for $\omega = 0.5$ and 1.0, respectively. The frictional and the centrifugal sideforces, c_{sf} and c_{ct}, partly compensate for each other. At lower spin rate, $\omega = 0.5$, the frictional force, c_{sf}, is larger than the centrifugal force, c_{ct} (figure 17a), resulting in a positive Magnus force, c_{Mg} (i.e., pointing to the right in figure 17a). At higher spin rate, $\omega = 1.0$, the opposite is obtained, i.e., the centrifugal force is larger in magnitude than the frictional force, and the Magnus force becomes negative (i.e., to the left in figure 17b).

The change of the Magnus force from positive at lower spin rate to negative at higher spin rate has been previously reported in a survey report by Jacobson (1975) who ascribed this change to wake vortices. Jacobson also provides an extensive literature of experiments on the Magnus effect not mentioned here. A series of flow-visualization pictures can be found in a report by Werle (1966).

4.9. The high-incidence problem

In the previous nonspinning, high-incidence work (Wang 1974a,b), calculations in the circumferential direction were carried out only up to the open separation lines. Determination of the leeside separated flow over the fore-body was attempted later, but the results have never been reported. That effort is included here as a part of the extension to the spinning, high-incidence problem.

For the nonspinning case, the calculation was extended into the region where the crossflow reverses. The resulting distributions for the skin frictions are shown in figure 18a. The meridional skin friction, $c_{f\mu}$,

shows a sharp decrease upon entering the reversed region from the windward direction and then increases somewhat toward the leeside symmetry plane $\theta = 180°$ (see $\mu = -0.88$ to $\mu = -0.86$). Such a trend intensifies so rapidly that $c_{f\mu}$ becomes zero at $\mu = -0.833$ and negative thereafter near $\theta = 140°$. The calculation was therefore terminated.

To put the matter into the right perspective, we should recall that in the nonspinning case for 6° incidence (Wang 1975), $c_{f\mu}$ was similarly found to decrease somewhat faster upon entering the reversed flow region from the windward side, but the variation in the longitudinal direction was so gradual that $c_{f\mu}$ did not become zero except on the aft-body, and the reversed flow region that extended over a quarter of the body length was calculated.

The quick termination at high incidence leads us to conclude that the leeside separated region associated with an open separation can not be determined according to the classical boundary layer theory. This is by no means an obvious conclusion from the outset, because it does not seem to be certain that the flow involved violates the boundary layer assumptions in any way, at least not on the upstream fore-body. Experience in the low incidence case just mentioned especially encourages one to think this way. In any case, the early termination for the high incidence is somewhat unexpected, presumably because the reversed flow is too strong and the boundary layer assumptions, such as one for potential pressure, are no longer valid.

The high-incidence problem is extended here to including the spinning motion for the following reasons: (1) to determine whether the boundary layer calculation can be started even though there is no rigorous way to obtain the initial profiles, (2) to find out whether spinning motion would change the

crossflow enough to extend the calculation farther downstream, and (3) to examine the flow features from solutions which can be obtained by the present simpler method, even for a limited region of the body surface.

In the previous nonspinning, high-incidence work, the problem involved first the calculation of the stagnation region, then the symmetry-plane solution, the nose-region solution, and finally the main-body solution. Spinning couples these local flows and hence, they cannot be determined separately in the order described. Currently, no simple rational way for resolving this question is known.

In the nonspinning case, different starting methods were used for the low-and high-incidence problems. For the high-incidence case, the starting method employed the nose-region solution as just mentioned. For the low incidence case, approximate profiles were made up using the justification that the boundary layer varies only slightly from the windside toward the leeside over the fore-body.

For the spinning case, the starting profiles for low incidence (6°) were described in §3.4a. The question then is whether the same technique can be employed for the high-incidence case. When this was tried, it was found (somewhat surprisingly) that the calculation proceeded downstream without difficulty. The starting station was located at $\mu = -0.943$, since the nonspinning solution for this particular, previously calculated μ-station was still available on tape. This nonspinning solution, modified by a pure spinning profile (figure 5), makes up the required initial profiles.

Two spinning cases with $\omega = 0.5$ and 1.0 are calculated for the same ellipsoid at 30° incidence. Over the fore-body, the cross-sectional radius is small, as is the spinning velocity of the body, v_B. It is noted that the

crossflow profiles at $\mu = -0.836$ exhibit some features similar to those in figure 8d, which is for $\mu = 0.40$ at 6° incidence. For example, at $\theta = 210°$ the v-velocity profile displays a non-monotonic reversed flow. The resulting crossflow pattern and the crossflow skin friction, $c_{f\theta}$, also suggest the same; namely: a similar crossflow over the aft-body at 6° incidence has already developed over the fore-body at 30° incidence.

The calculated meridional skin friction, $c_{f\mu}$, for $\alpha = 30°$ and $\omega = 0.5$ is shown in figure 18b. Compared to figure 12 for 6° incidence, the $c_{f\mu}$ distribution along a fixed μ-station changes noticeably within a short longitudinal distance (from $\mu = -0.940$ to $\mu = -0.833$). Along $\mu = -0.87$ or -0.85, $c_{f\mu}$ increases from $\theta = 0°$ to $\theta = 90° \sim 100°$, decreases sharply around $\theta = 140°$, $\sim 160°$, then increases again slightly up to $\theta = 220° \sim 240°$. Around $\theta = 250°$, a second dip appears. At $\mu = -0.833$, $c_{f\mu}$ drops almost to zero at $\theta = 160°$ so that the present calculation must be terminated. This occurs at the same μ-station as for the nonspinning case. Increase of the spin rate to $\omega = 1.0$ enables the calculation to be extended downstream slightly (terminated at $\mu = -0.812$), but otherwise, the same characteristics prevail.

Thus, the question of initial profiles did not present an insurmountable problem, but calculation could not be continued in the longitudinal direction for very far after the point at which an open separation for the corresponding nonspinning case occurs. Since the starting point of open separation continues to move upstream as the incidence increases (Wang 1976), this means that the area over which the spinning boundary layer can be calculated decreases at higher incidence. The source of difficulty is in the leeside region associated with an open separation where a classical boundary layer treatment is shown to be inadequate. In the nonspinning case, calculation from

the windward side may be stopped at the open separation line with the leeside region left undetermined. In the spinning case, the calculation must be carried through the leeside region and around the whole cross section in order to march downstream. Inability to determine the leeside region flow prevents the downstream calculation.

In the parabolicized Navier-Stokes approach (Lin & Rubin 1974), the pressure distribution is assumed in the same way as it is in the boundary layer theory. On this basis, it is doubtful that the parabolicized Navier-Stokes approach can do better with respect to the leeside flow discussed above. In either approach, it is believed that more realistic experimental pressure distribution would be helpful.

5. CONCLUSIONS

The three-dimensional laminar boundary layer over a spinning blunt-body of revolution at incidence is investigated here. Complete, concrete results are obtained for an ellipsoid of revolution, which provides a model of more general geometry than the sharp cone studied before. Spinning introduces unique features in both fluid mechanics and methodology.

Spinning causes asymmetry which, in turn, results in the side-forces known as Magnus effects. The asymmetry is most pronounced in the crossflow, but the meridional flow is also affected through the coupling, as evidenced in the asymmetrical distribution of $c_{f\mu}$ and Δ^*_μ. The variety of crossflow profiles found is greater than usually encountered in any single flow problem. The calculated flow patterns in the cross-and meridional-planes provide a clear picture of the flow structure. In particular, the cross-plane flow patterns and the singularities involved are presented in detail, along with the skin frictions and displacement thicknesses. A negative displacement thickness is found to be physically meaningful in the spinning-body boundary layer, although its effect on the overall flow is negligible in the case calculated. The Magnus forces due to the circumferential skin friction and the centrifugal pressure are determined; these two forces partly compensate for each other. At lower spin rates, the frictional force is larger, resulting in a positive Magnus force. At higher spin rates, the opposite is the case. The overall magnitude of the Magnus force increases with spin rate. At high incidence (30°), boundary layer calculations are carried out in the longitudinal direction only up to where an open separation occurs. The leeside separated region associated with an open separation is not amenable to a classical boundary layer treatment. The flow characteristics, which occur on the aft-body just ahead

of separation at 6° incidence, are found to already prevail over the forebody at 30° incidence.

Methodologically, the present work strictly follows the boundary layer theory, which does not become invalid merely because of the presence of the crossflow reversal. The associated zone of dependence can be effectively observed with the Krause scheme. The generation of initial profiles to start the calculation did not lead to the previously expected impasse. Profiles for longitudinal marching can be approximated by superimposing the corresponding nonspinning profile on an assumed pure spinning profile. The profiles for circumferential marching are generated as the computation proceeds. The present calculation terminates when the meridional skin friction, $c_{f\mu}$, becomes zero, because the boundary layer theory ceases to be valid when both the u- and the v-profiles reverse. In this respect, the parabolicized Navier-Stokes approach offers no advantage.

This work was supported by the U. S. Army Research Office under Contract No. DAHC04-73-C-0011, and by the U. S. Air Force Office of Scientific Research under Contract F49620-76-C-0004. The author is greatly indebted to Susan Yamamura and Richard Showers for their assistance in developing the computer program and obtaining the results.

REFERENCES

Clark, B. L. 1972. AIAA Paper 72-112.

Dwyer, H. A. 1968. AIAA J. 6(7), 1336-1342.

Dwyer, H. A. 1971. AIAA Paper 71-57.

Dwyer, H. A. & Sanders, B. R. 1976. AIAA J. 14(4), 498-504.

Hall, M. G. 1967. Royal Aircraft Establishment TR 6714.

Jacobson, I.D. 1975. AGARDograph No. 171.

Kelley, H. R. 1954. Naval Ord. Test Station TM-1634.

Kitchens, C. W. Jr., Gerber, N., & Sedney, R. 1975. Ballistics Research Labs. Rep. No. 1774.

Krause, E. 1969. AIAA J. 7(3), 575-576.

Lighthill, M. J. 1958. J. Fluid Mech. 4(4), 383-392.

Lin, T. C. & Rubin, S. G. 1974. AIAA J. 12(7), 975-985.

Martin, J. C. 1957. J. Aero. Sci. 24(6), 421-429.

Moore, F. K. 1953. NACA TR 1124.

Prandtl, L. 1952. The Essentials of Fluid Dynamics. p. 71. Blackie and Son limited, London.

Richtmyer, R. D. & Morton, K. W. 1967. Difference Methods for Initial-Value Problems. John Wiley & Sons, Inc. N. Y.

Sanders, B.R. & Dwyer, H. A. 1976. AIAA J. 14(5), 576-582.

Sedney, R. 1957. J. Aero. Sci. 24(6), 430-436.

Vaughn, H. R. & Reis, G. E. 1973. AIAA Paper 73-124.

Wang, K. C. 1974a. Proc. Royal Soc. Longon A. 340, 33-55.

Wang, K. C. 1974b. Phys. of Fluids 17(7), 1381-1385.

Wang, K. D. 1975. J. Fluid Mech. 72(1), 49-65.

Wang, K. C. 1976. Proc. of the Viscous Flow Symposium, Lockheed-Georgia Co. Atlanta, Ga. LG77ER0044, 341-414. Also Martin Marietta Labs. TR-76-54c.

Wang, K. C. 1977. Martin Marietta Labs. TR-77-50c.

Watkins, C. B. 1973a. AIAA J. 11(4), 559-561.

Watkins, C. B. 1973b. Computers & Fluids, 1(4), 317-329.

Werle, H. 1966. ONERA document No. 71/1859A.

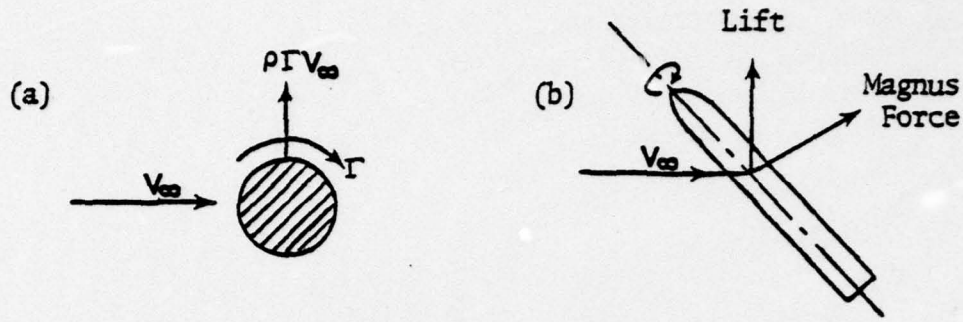

Figure 1. Magnus force. (a) two-dimensional; (b) three-dimensional.

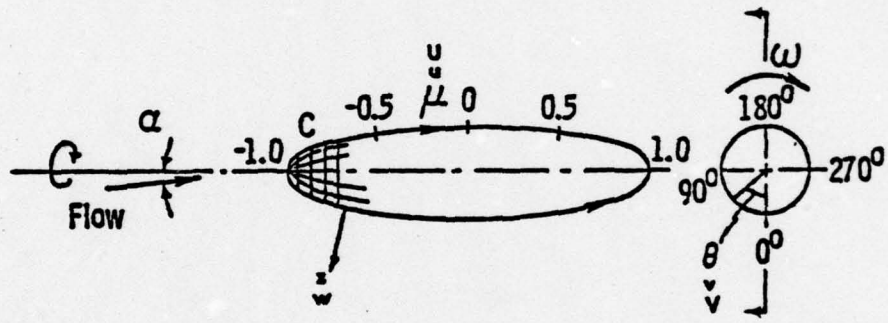

Figure 2. Geometry and coordinates.

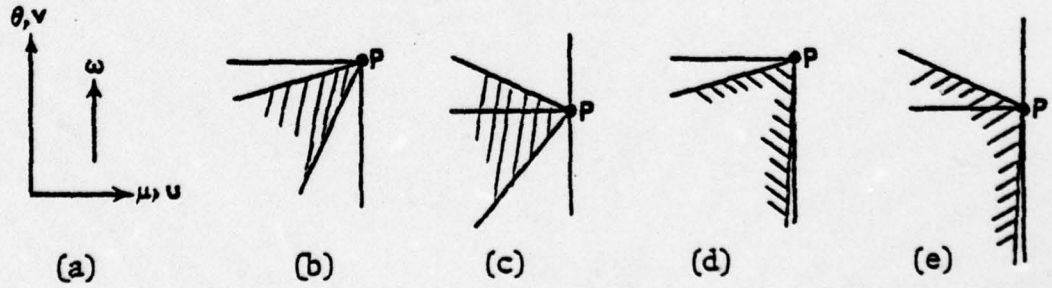

Figure 3. The zone of dependence. (a) coordinates; (b) nonspinning, no reversal; (c) nonspinning, reversal; (d) spinning, no reversal; (e) spinning, reversal.

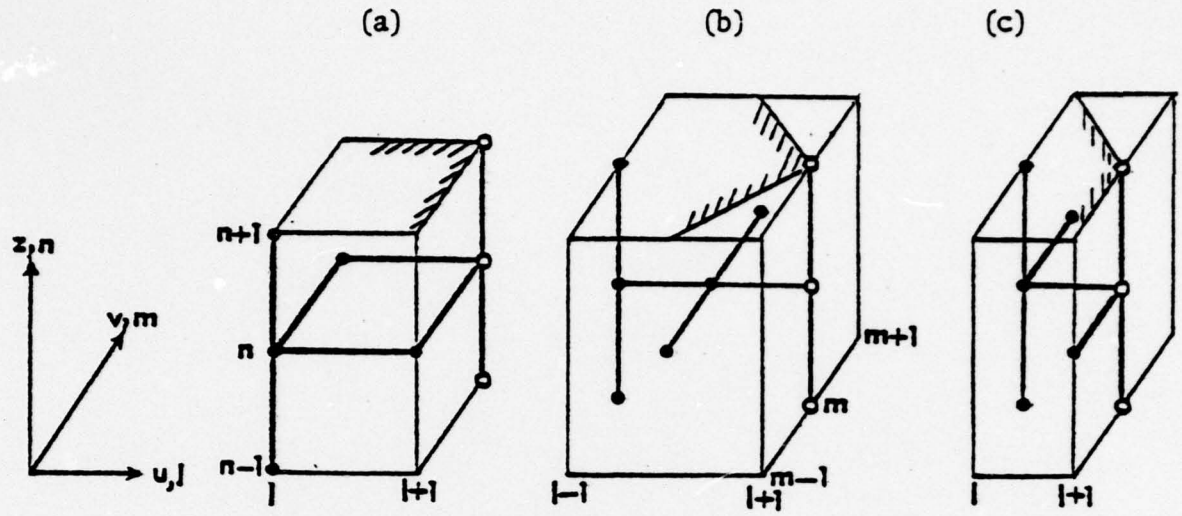

Figure 4. Difference meshes for momentum equations.
(a) scheme 1; (b) scheme 2; (c) scheme 3.

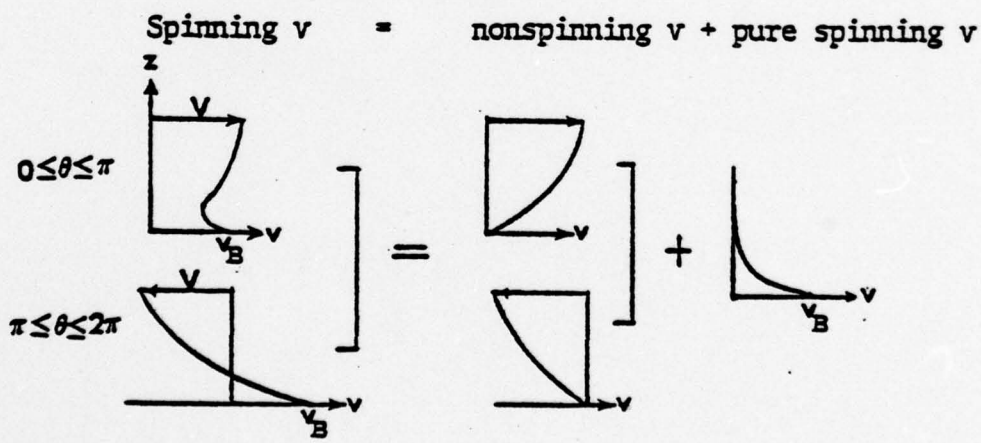

Figure 5. Initial profile for meridional marching.

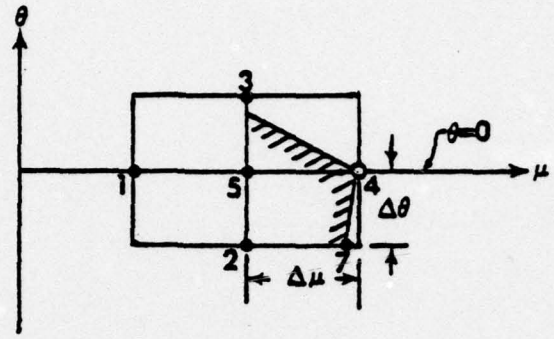

Figure 6. Initial profile for circumferential marching.

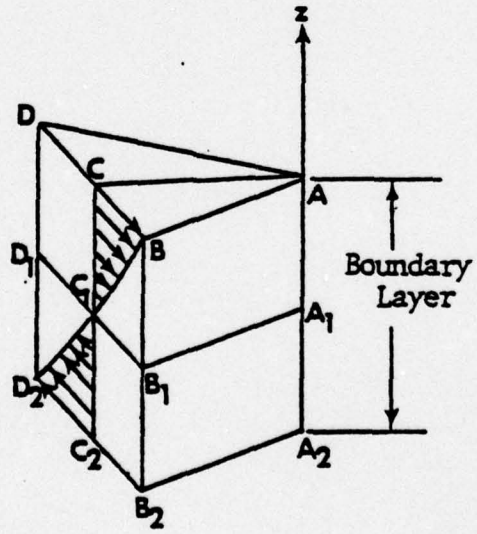

Figure 7. Dependence zone for Dwyer and Sanders' scheme.

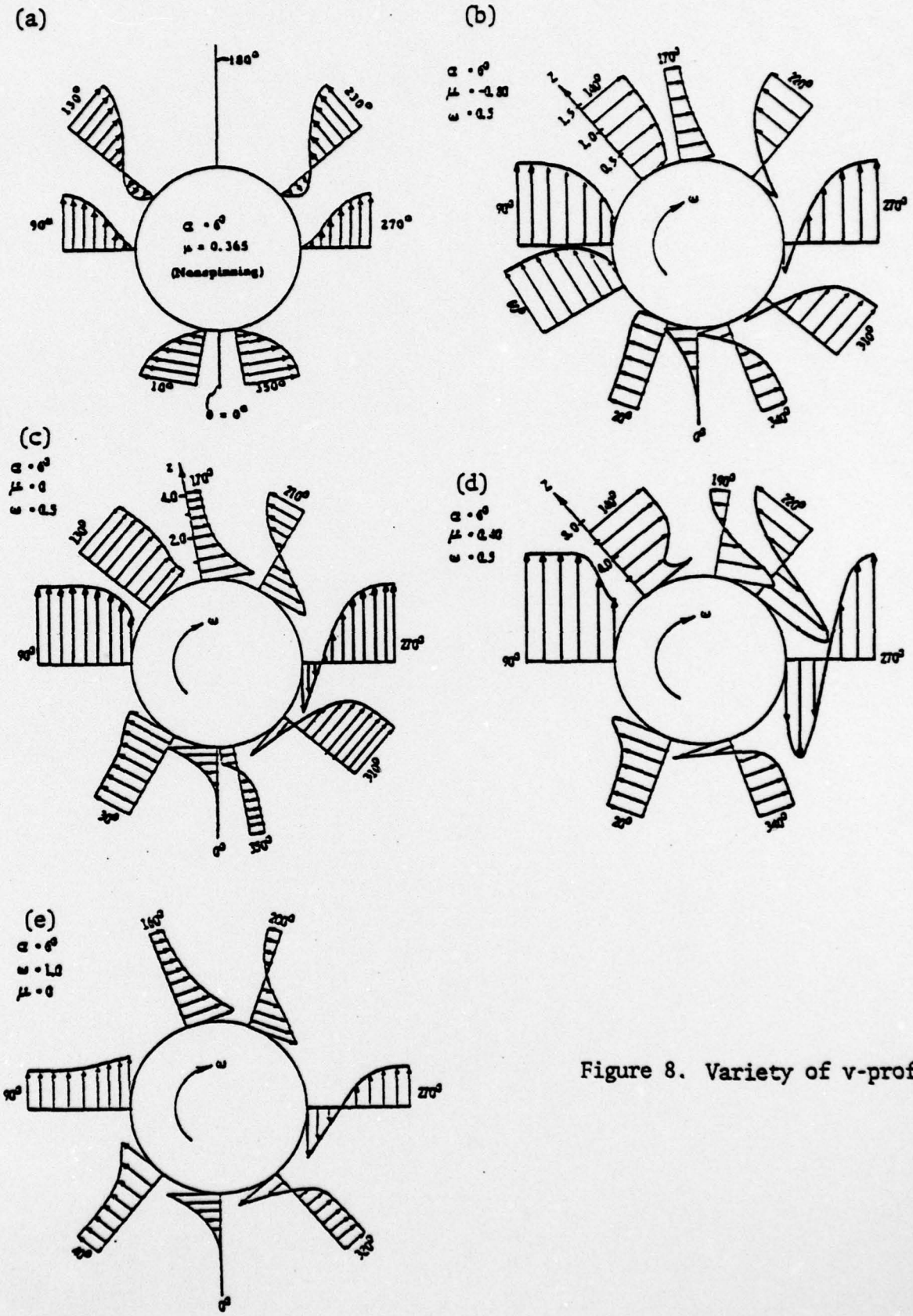

Figure 8. Variety of v-profile.

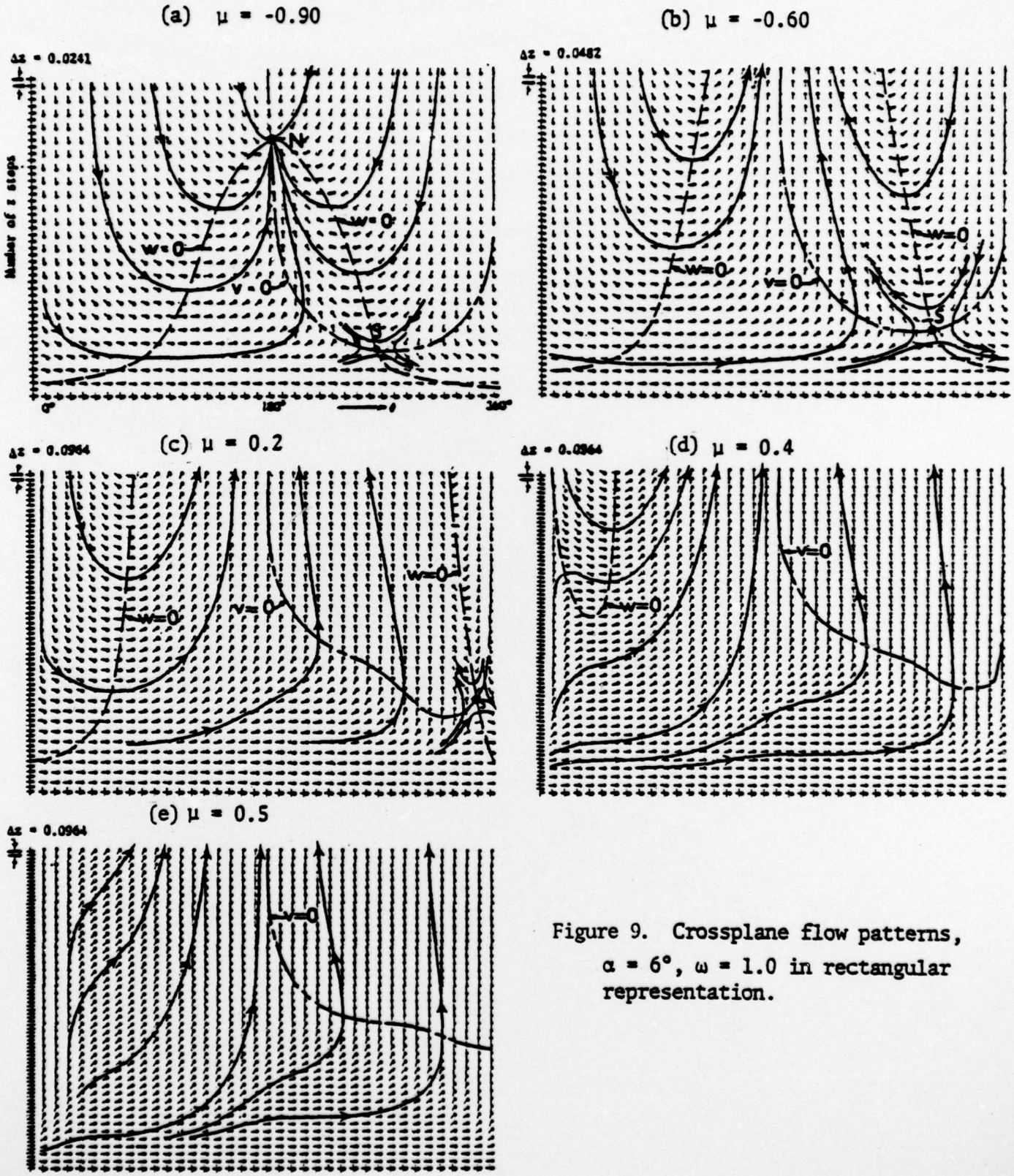

Figure 9. Crossplane flow patterns, $\alpha = 6°$, $\omega = 1.0$ in rectangular representation.

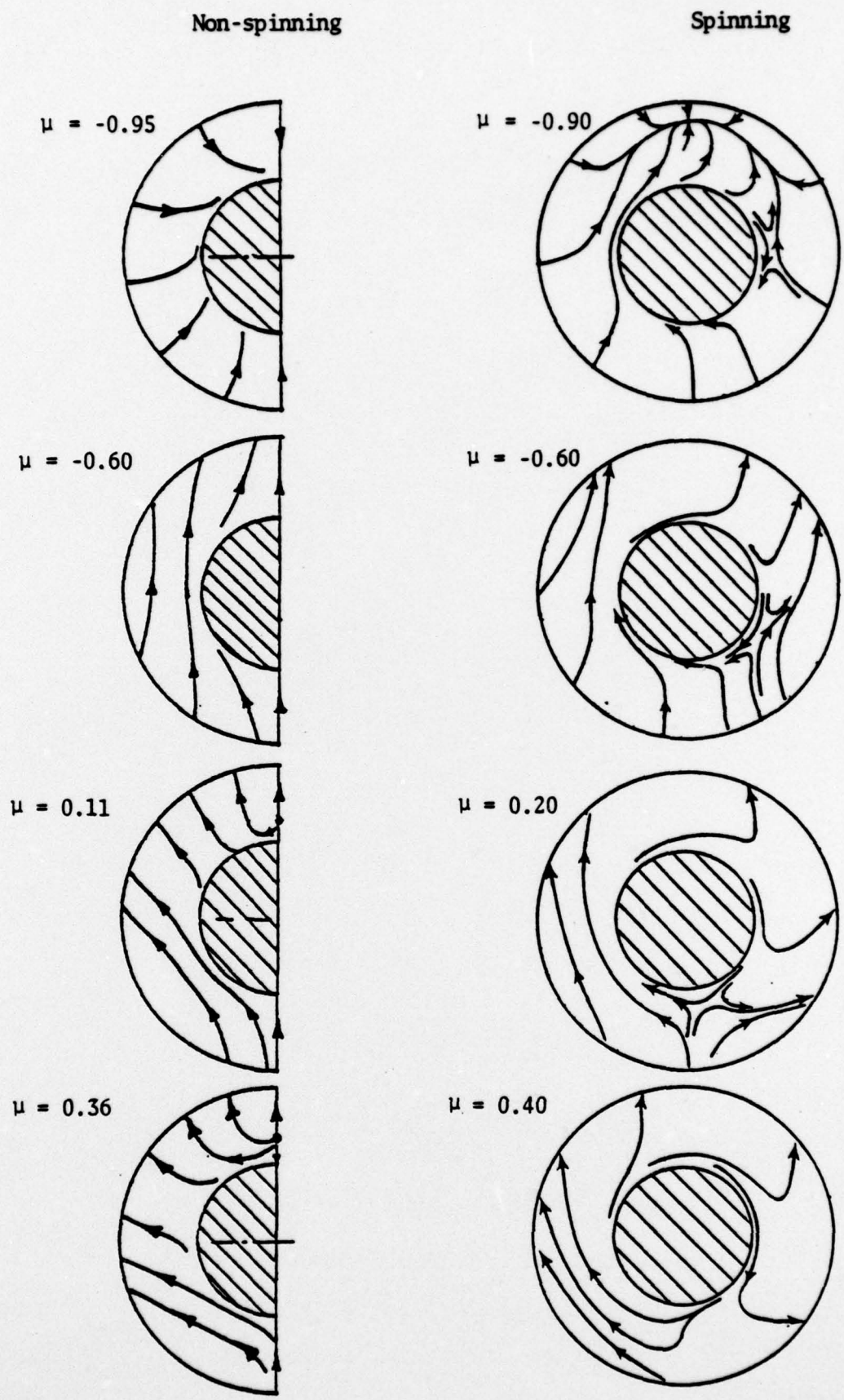

Figure 10. Comparison of cross-flow patterns in polar representation.

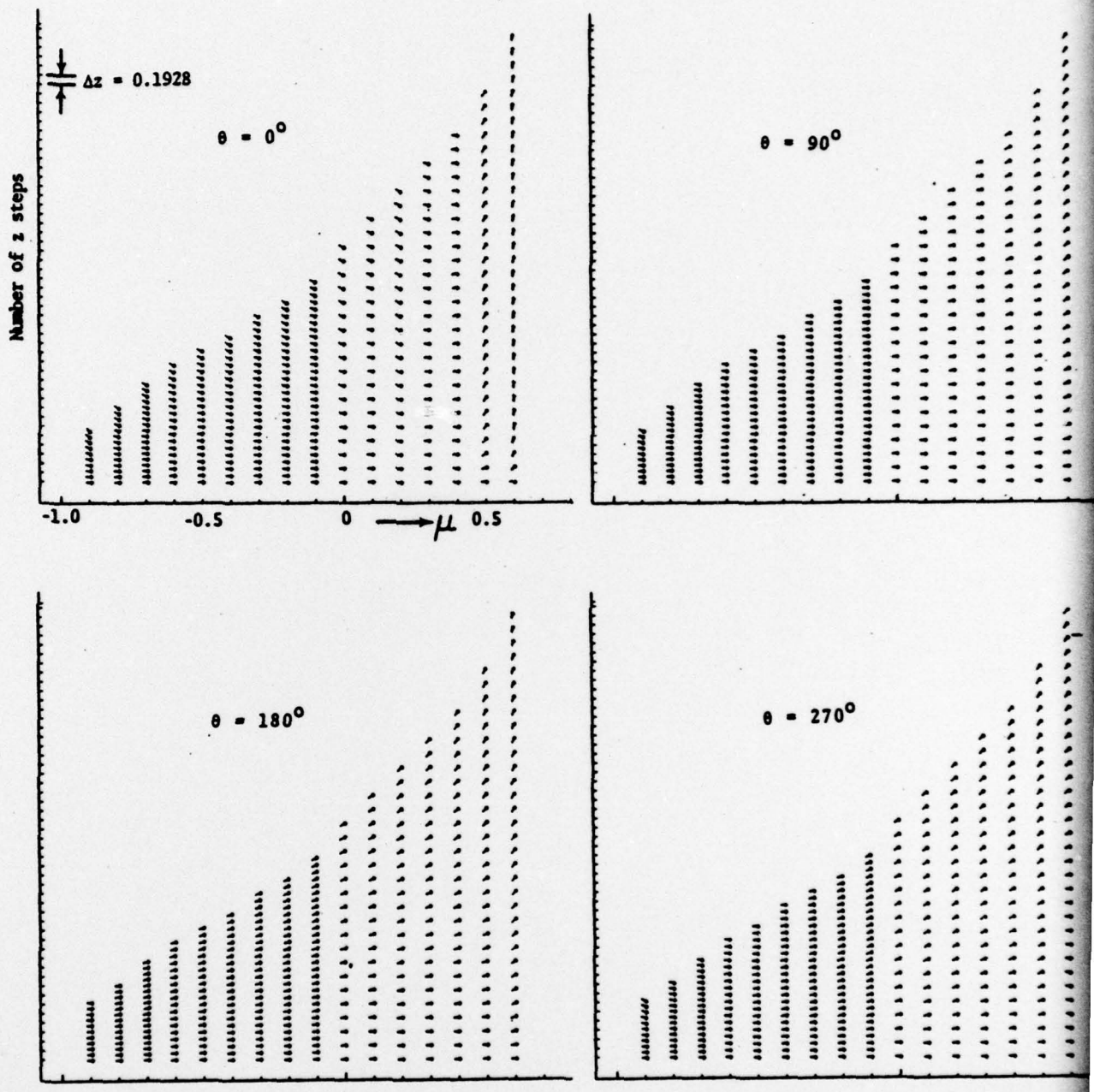

Figure 11. Meridional-plane flow patterns, $\alpha = 6°$, $\omega = 1.0$.

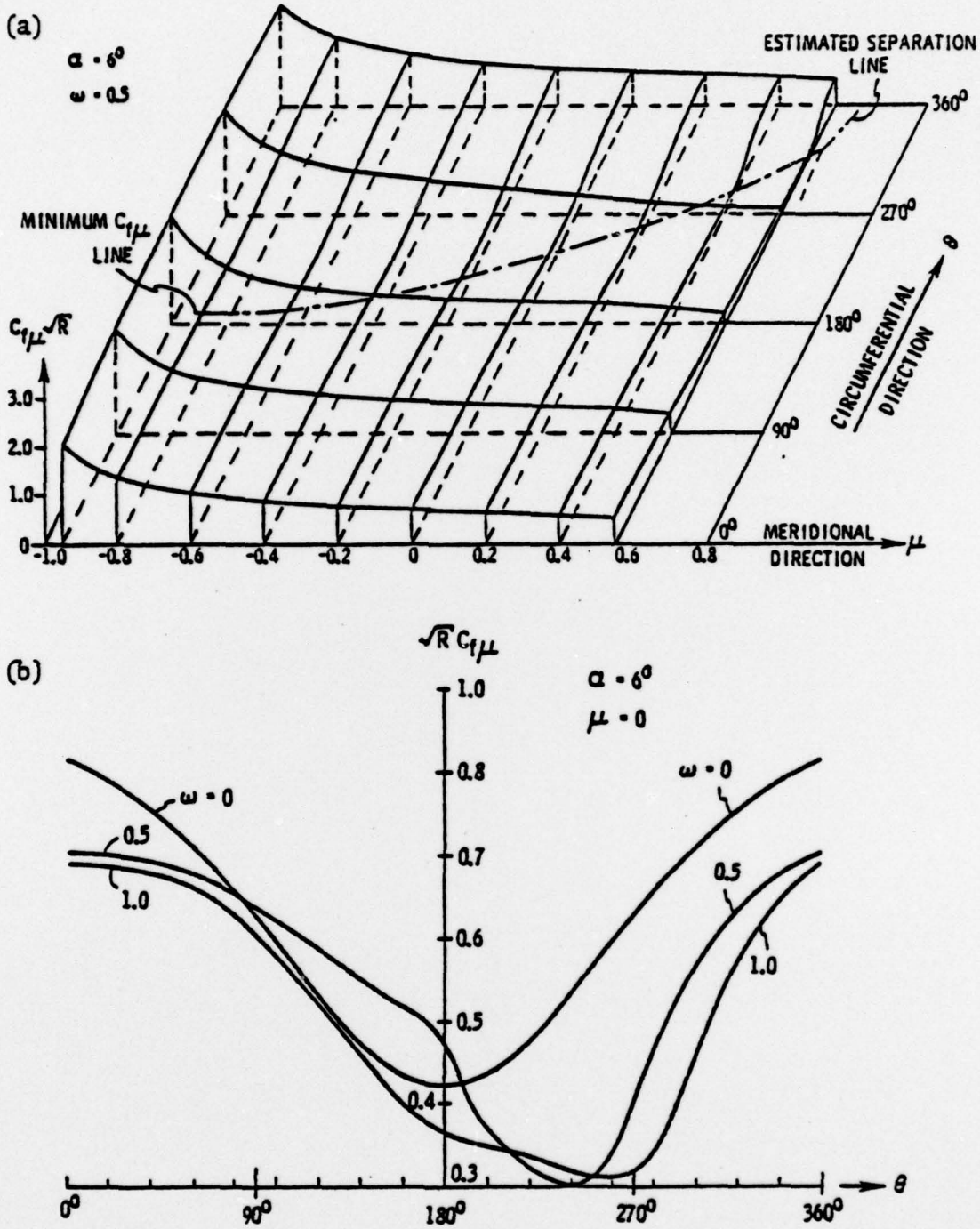

Figure 12. Meridional skin friction, $c_{f\mu}$. (a) Distribution of $c_{f\mu}$, $\omega = 0.5$; (b) Comparison of $c_{f\mu}$ for different ω's.

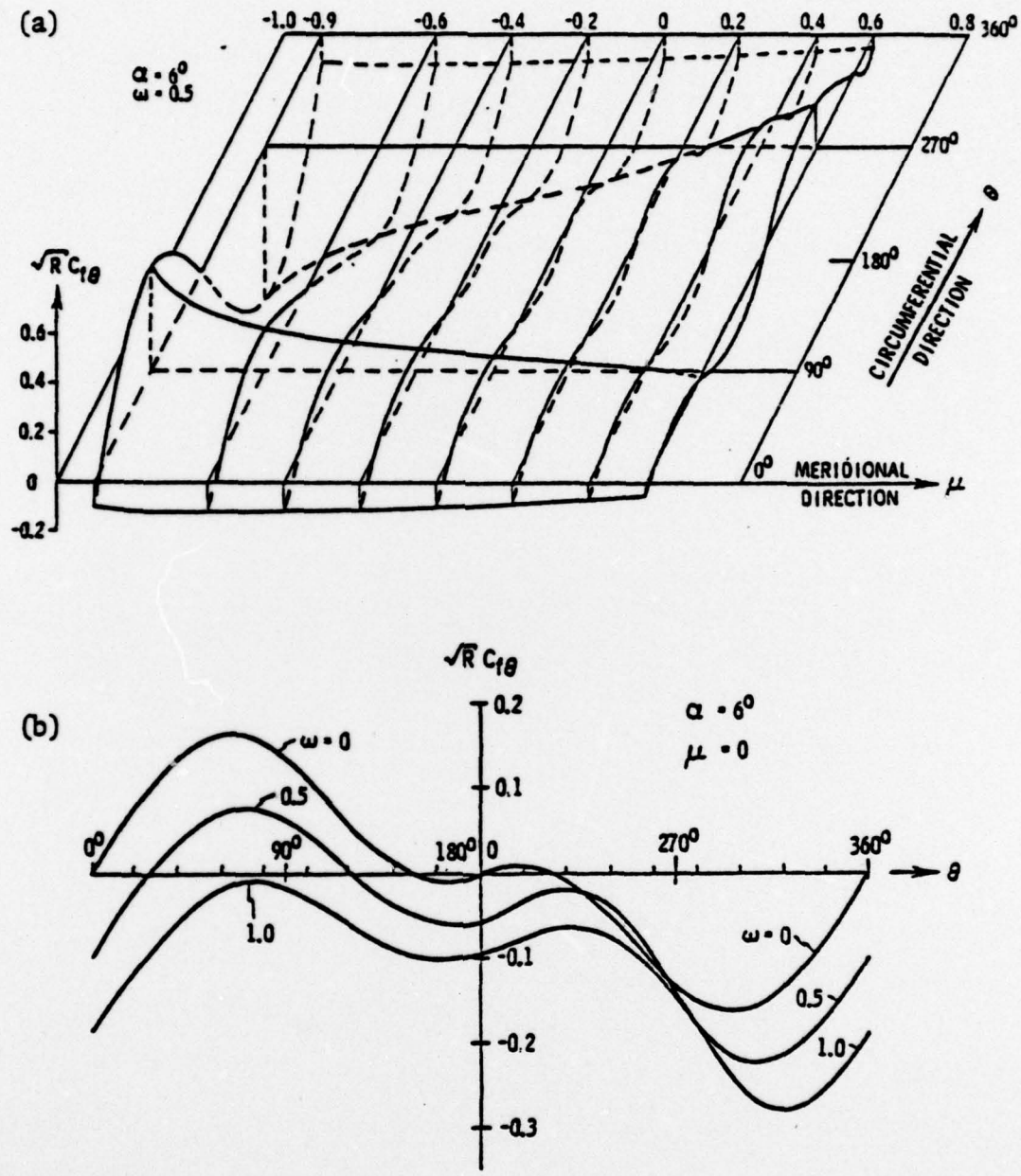

Figure 13. Circumferential skin friction, $c_{f\theta}$. (a) Distribution of $c_{f\theta}$, $\omega = 0.5$; (b) Comparison of $c_{f\theta}$ for different ω's.

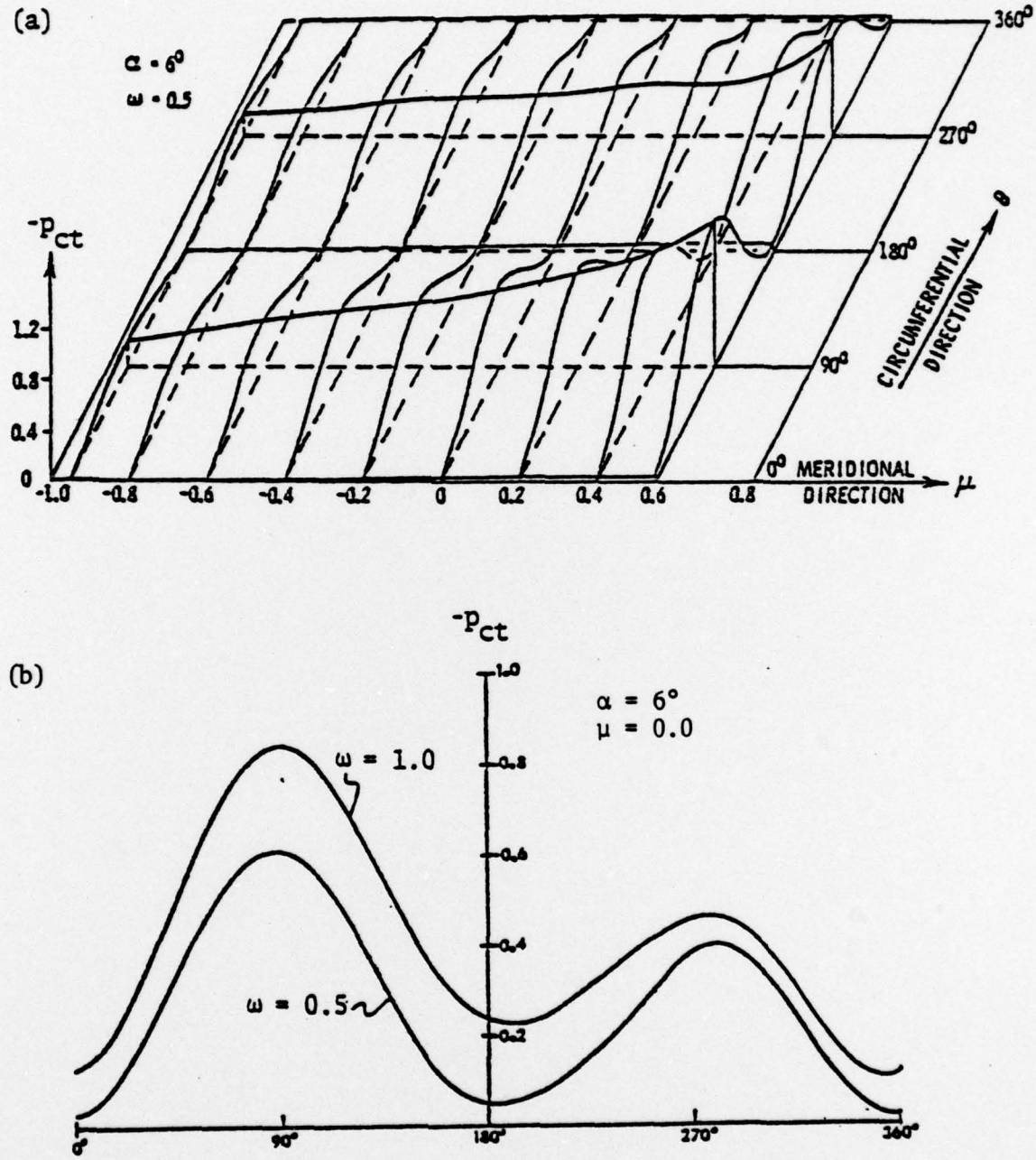

Figure 14. Centrifugal pressure, p_{ct}. (a) Distribution of p_{ct}, $\omega = 0.5$; (b) Comparison of p_{ct} for different ω's.

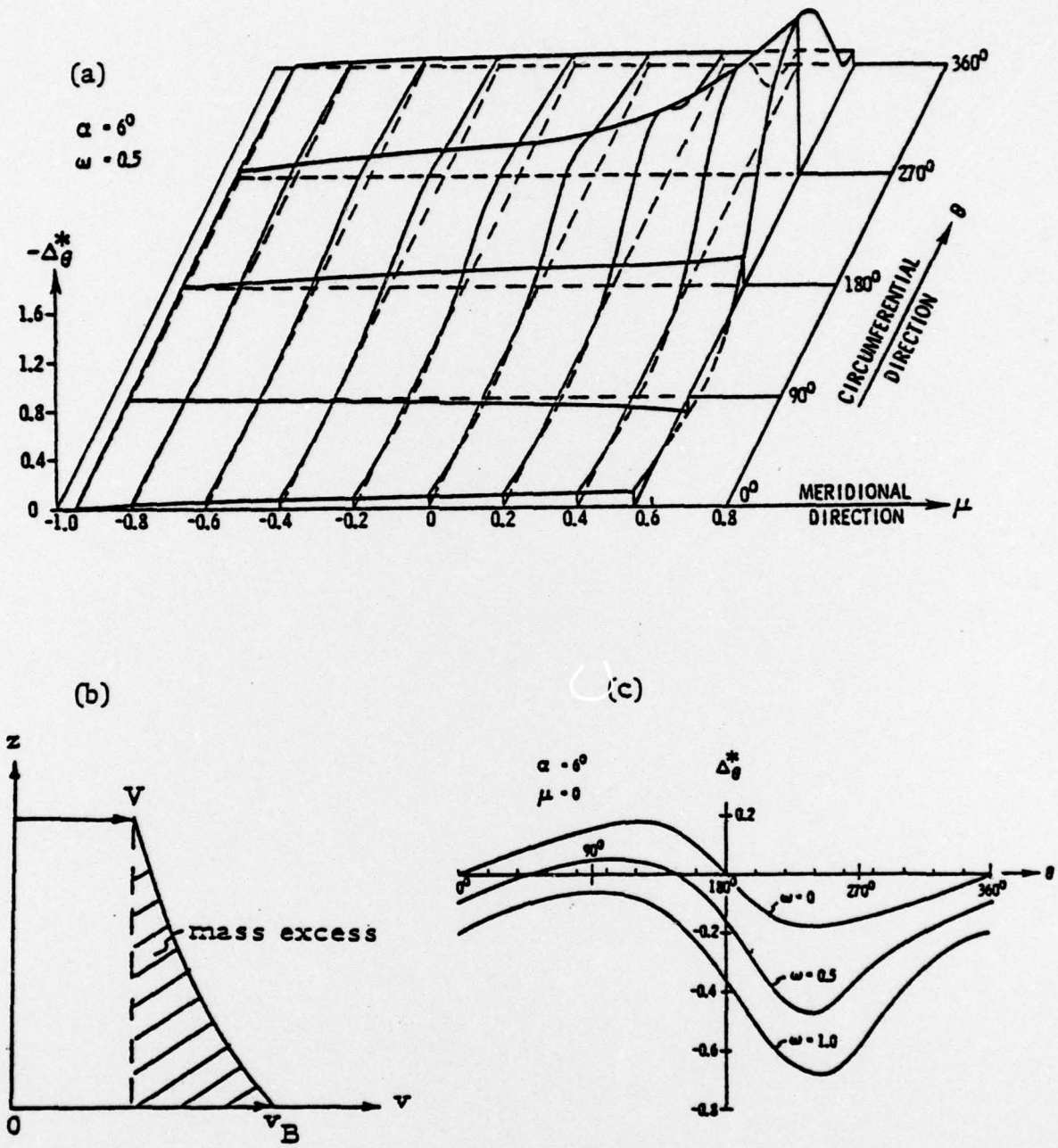

Figure 15. v-velocity displacement thickness, Δ_θ^*.
(a) Distribution of Δ_θ^*; (b) Physically negative Δ_θ^*;
(c) Comparison of Δ_θ^* for different ω's.

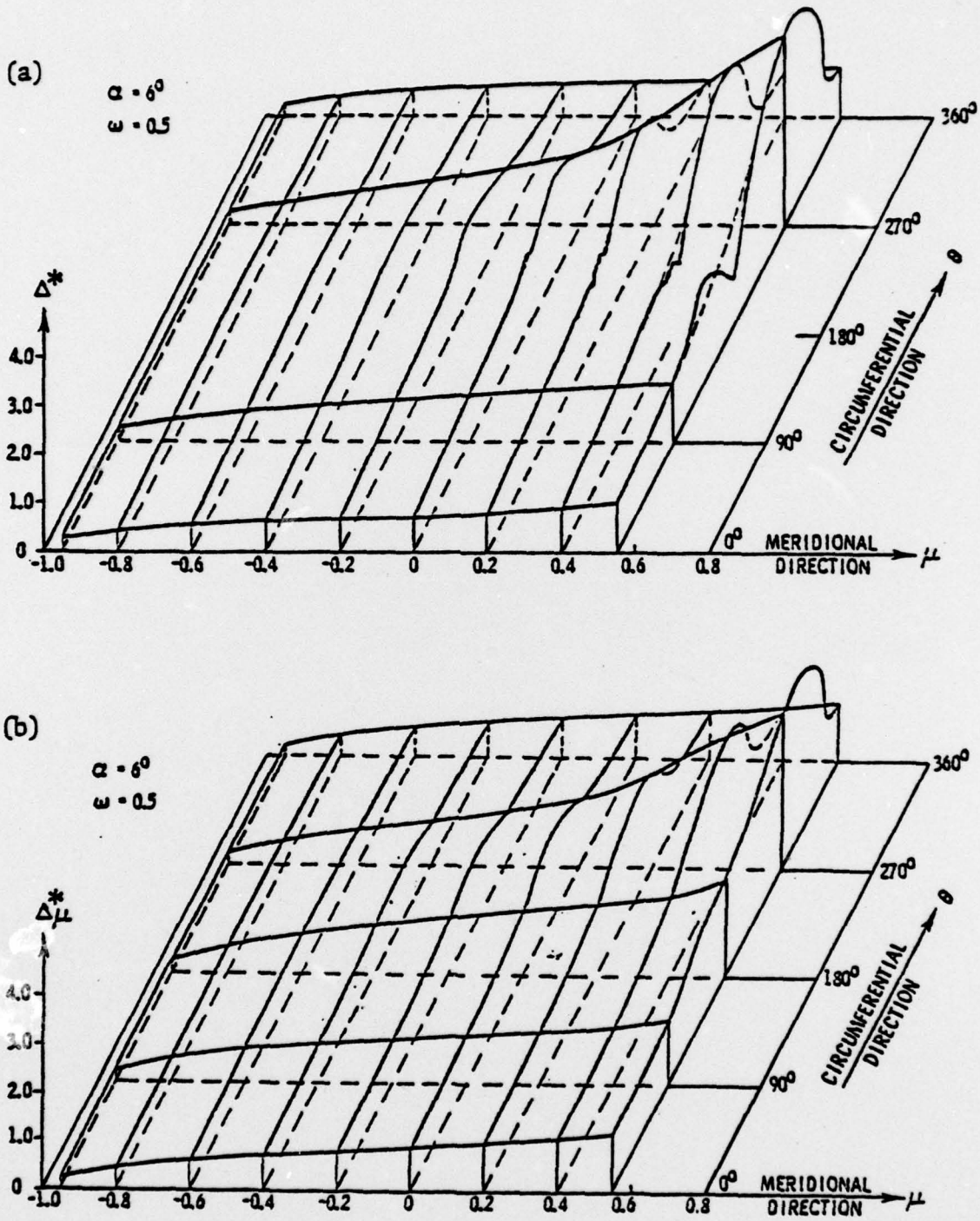

Figure 16. Displacement thickness. (a) total displacement thickness, Δ^*; (b) u-velocity displacement thickness, Δ^*_μ .

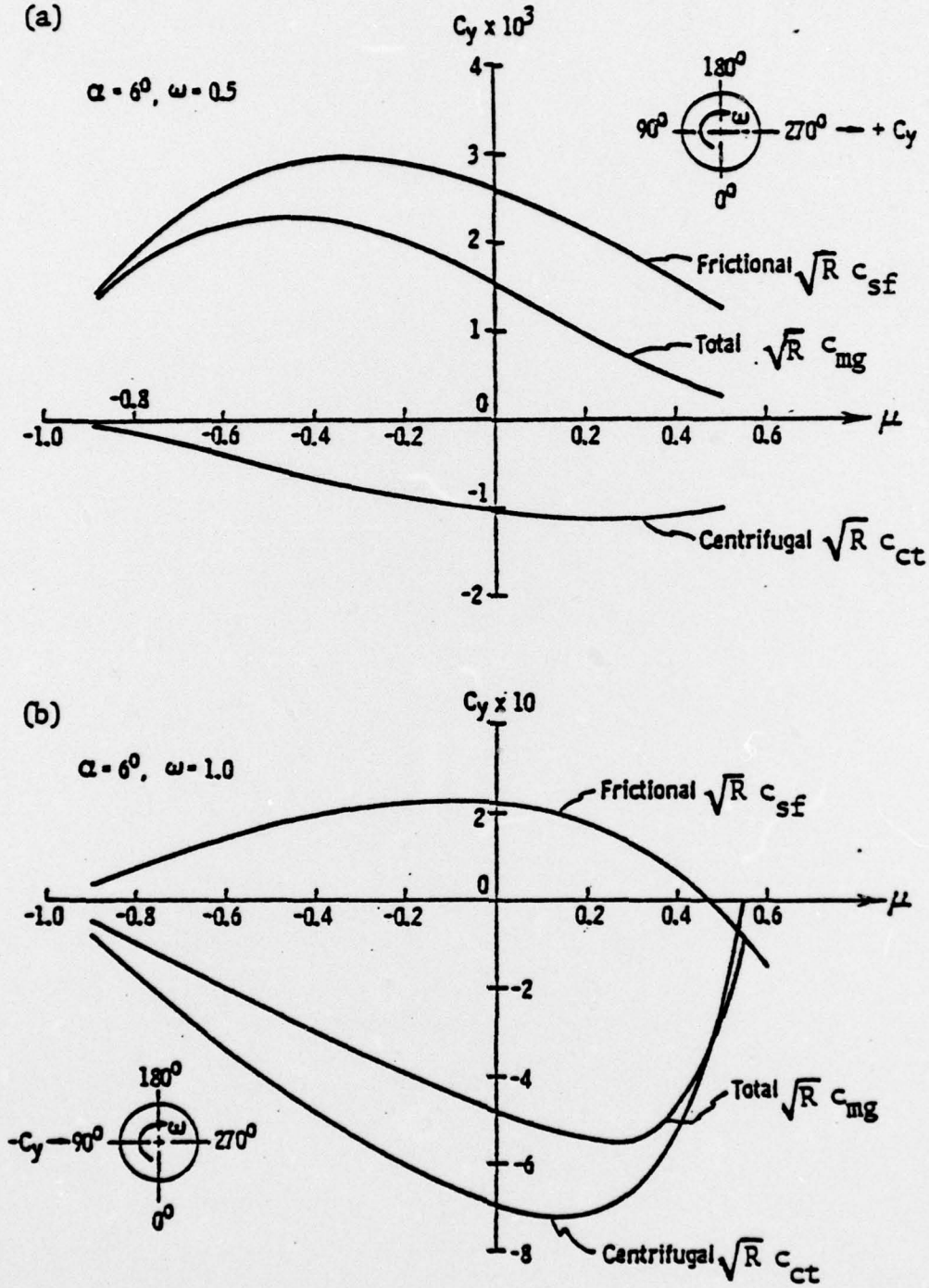

Figure 17. Sectional side-force.

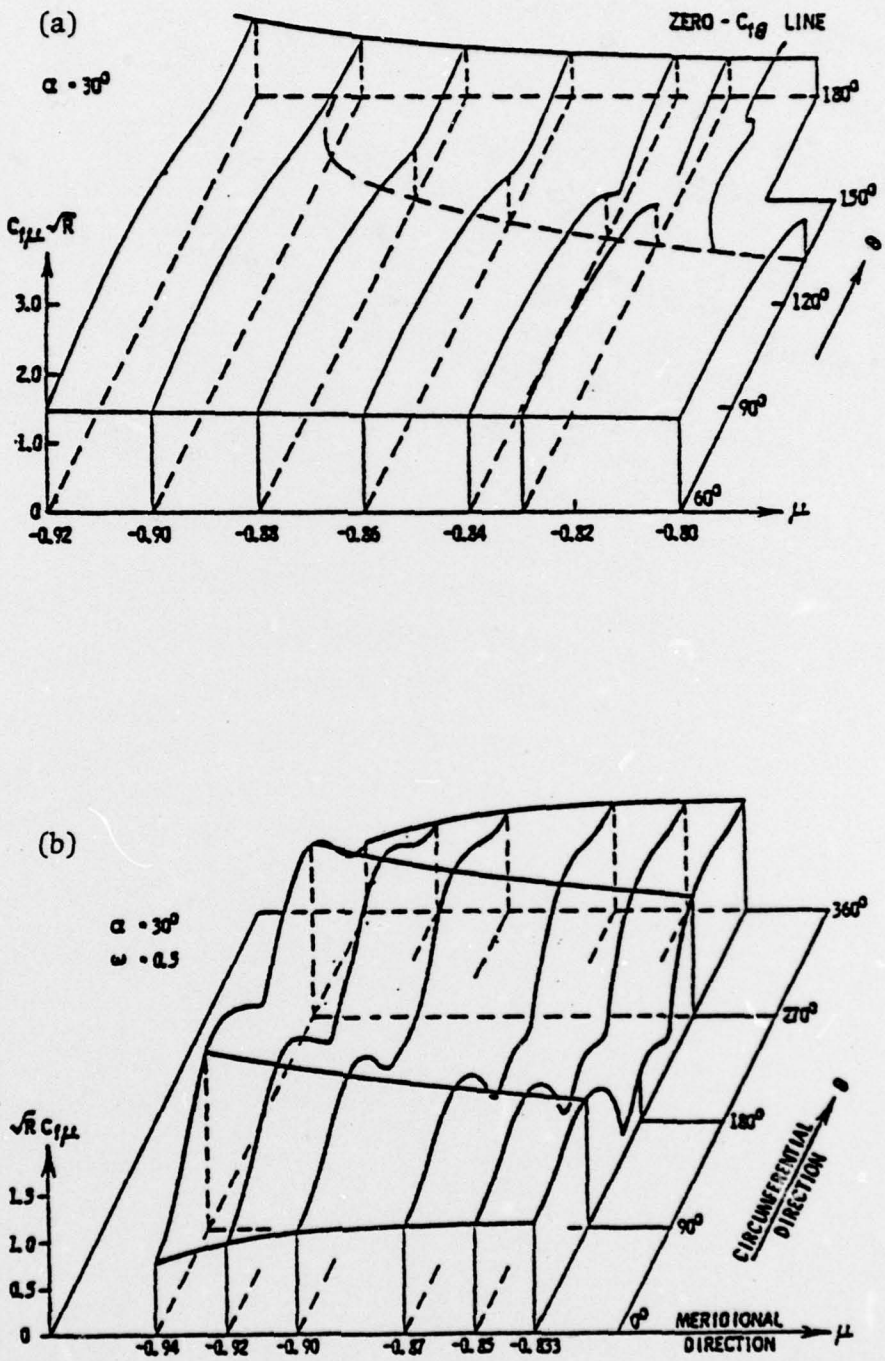

Figure 18. Meridional skin friction at 30° incidence.
(a) ω = 0; (b) ω = 0.5.

List of Figure Captions

Figure 1. Magnus force. (a) two-dimensional; (b) three-dimensional.

Figure 2. Geometry and coordinates.

Figure 3. The zone of dependence. (a) coordinates; (b) nonspinning, no reversal; (c) nonspinning, reversal; (d) spinning, no reversal; (e) spinning, reversal.

Figure 4. Difference meshes for momentum equations. (a) scheme 1; (b) scheme 2; (c) scheme 3.

Figure 5. Initial profile for meridional marching.

Figure 6. Initial profile for circumferential marching.

Figure 7. Dependence zone for Dwyer and Sanders' scheme.

Figure 8. Variety of v-profile.

Figure 9. Crossplane flow patterns, $\alpha = 6°$, $\omega = 1.0$ in rectangular representation.

Figure 10. Comparison of cross-flow patterns in polar representation.

Figure 11. Meridional-plane flow patterns, $\alpha = 6°$, $\omega = 1.0$.

Figure 12. Meridional skin friction, $c_{f\mu}$. (a) Distribution of $c_{f\mu}$, (b) Comparison of $c_{f\mu}$ for different ω's.

Figure 13. Circumferential skin friction, $c_{f\theta}$. (a) Distribution of $c_{f\theta}$, $\omega = 0.5$; (b) Comparison of $c_{f\theta}$ for different ω's.

Figure 14. Centrifugal pressure, p_{ct}. (a) Distribution of p_{ct}, $\omega = 0.5$; (b) Comparison of p_{ct} for different ω's.

Figure 15. v-velocity displacement thickness, Δ_θ^*. (a) Distribution of Δ_θ^*; (b) Physically negative Δ_θ^*; (c) Comparison of Δ_θ^* for different ω's.

Figure 16. Displacement thickness. (a) total displacement thickness, Δ^*; (b) u-velocity displacement thickness, Δ_μ^*.

Figure 17. Sectional side-force.

Figure 18. Meridional skin friction at 30° incidence. (a) $\omega = 0$; (b) $\omega = 0.5$.

SECURITY CLASSIFICATION OF THIS PAGE (When Data Entered)

REPORT DOCUMENTATION PAGE

READ INSTRUCTIONS BEFORE COMPLETING FORM

1. REPORT NUMBER: 18 AFOSR-TR-77-1306 (19)

2. GOVT ACCESSION NO.

3. RECIPIENT'S CATALOG NUMBER

4. TITLE (and Subtitle): 6 BOUNDARY LAYER OVER SPINNING BLUNT-BODY OF REVOLUTION AT INCIDENCE INCLUDING MAGNUS FORCES,

5. TYPE OF REPORT & PERIOD COVERED: Interim

6. PERFORMING ORG. REPORT NUMBER

7. AUTHOR(s): 10 K. C. Wang

8. CONTRACT OR GRANT NUMBER(s): 15 F49620-76-C-0004

9. PERFORMING ORGANIZATION NAME AND ADDRESS:
~~Martin Marietta Corporation~~
Martin Marietta Laboratories
1450 South Rolling Road
~~Baltimore, Maryland 21227~~

10. PROGRAM ELEMENT, PROJECT, TASK AREA & WORK UNIT NUMBERS: 61102F 2304 A3 (16) (17)

11. CONTROLLING OFFICE NAME AND ADDRESS:
Air Force Office of Scientific Research/NM
Bolling AFB, DC 20332

12. REPORT DATE: 11 1977

13. NUMBER OF PAGES: ~~51~~ 12 55p.

14. MONITORING AGENCY NAME & ADDRESS (if different from Controlling Office)

15. SECURITY CLASS. (of this report): Unclassified

15a. DECLASSIFICATION/DOWNGRADING SCHEDULE

16. DISTRIBUTION STATEMENT (of this Report)

Approved for public release; distribution unlimited.

17. DISTRIBUTION STATEMENT (of the abstract entered in Block 20, if different from Report)

18. SUPPLEMENTARY NOTES

19. KEY WORDS (Continue on reverse side if necessary and identify by block number)
Three-dimensional boundary layer
Boundary layer over spinning-body at incidence
Magnus forces
Numerical solutions

20. ABSTRACT (Continue on reverse side if necessary and identify by block number)

An incompressible laminar flow over a spinning blunt-body at incidence is investigated. The approach follows strictly the three-dimensional boundary layer theory, and the lack of initial profiles is readily resolved. The rule of the dependence zone is satisfied with the Krause scheme and complete numerical solutions are obtained for an ellipsoid of revolution at 6° incidences and two different spin rates. Spinning causes asymmetry which, in

DD FORM 1 JAN 73 1473 EDITION OF 1 NOV 65 IS OBSOLETE

UNCLASSIFIED

SECURITY CLASSIFICATION OF THIS PAGE (When Data Entered)

407998

20. Abstract

turn, introduces the Magnus force. The asymmetry is most pronounced in crossflow, but is also noticeable in the skin-friction and displacement thickness of the meridional flow. A variety of crossflow profiles are determined as are the streamline patterns in the cross- and meridional-planes which are especially useful in visualizing the flow structure. Detailed distribution of skin frictions, displacement thicknesses, and centrifugal pressure are presented. A new derivation of the total displacement thickness is given and a negative displacement thickness is found physically meaningful. The Magnus forces due to the crossflow skin friction and the centrifugal pressure are determined; these two forces partly compensate each other. At lower spin rate, the frictional force is larger, resulting in a positive Magnus force. At high spin rate, the opposite is obtained. At high incidence (30°), the leeside separated region associated with an open separation is found not ameanable to a classical boundary layer treatment. The present boundary layer calculations could be carried out, in the longitudinal direction, only up to the beginning of an open separation. Since an open separation moves forward with increasing incidence, the calculable area, therefore, decreases.

deg